

# The Impact of Plate Motions on Long-Wavelength InSAR-Derived Velocity Fields

Oliver L Stephenson<sup>1,1</sup>, Yuan-Kai Liu<sup>1,1</sup>, Zhang Yunjun<sup>2,2</sup>, Mark Simons<sup>1,1</sup>, Paul A Rosen<sup>2,2</sup>, and Xiaohua Xu<sup>3</sup>

<sup>1</sup>Caltech

<sup>2</sup>California Institute of Technology

<sup>3</sup>The University of Texas at Austin

November 30, 2022

## Abstract

Interferometric Synthetic Aperture Radar (InSAR) measurements are increasingly being used to measure small amplitude tectonic deformations over large spatial scales. Residual signals are often present at these scales, and are interpreted to be noise of indeterminate origin, limiting studies of long-wavelength deformation. Here, we demonstrate the impact of bulk motion by the Earth's tectonic plates on InSAR-derived velocity fields. The range-dependent incidence angle of the InSAR observations, coupled with plate velocities of centimeters per year, can induce long-wavelength spatial gradients of millimeters per year over hundreds of kilometers in InSAR-derived velocity fields. We show that, after applying corrections, including for the ionosphere and troposphere, plate motion represents the dominant source of long-wavelength secular velocity gradients in multi-year time series for several study areas. This signal can be accounted for using plate motion models, allowing improved detection of regional tectonic strain at continental scales.

# The Impact of Plate Motions on Long-Wavelength InSAR-Derived Velocity Fields

Oliver L. Stephenson<sup>1</sup>, Yuan-Kai Liu<sup>1</sup>, Zhang Yunjun<sup>1</sup>, Mark Simons<sup>1</sup>,  
Paul Rosen<sup>2</sup>, and Xiaohua Xu<sup>3</sup>

<sup>1</sup>Seismological Laboratory, Division of Geological and Planetary Sciences, California Institute of  
Technology, Pasadena, CA 91125, USA.

<sup>2</sup>Jet Propulsion Laboratory, California Institute of Technology, Pasadena, CA 91109, USA.

<sup>3</sup>Institute for Geophysics, University of Texas at Austin, Austin, TX 78758, USA.

## Key Points:

- Interferometric synthetic aperture radar (InSAR) time series are sensitive to uniform horizontal and vertical plate motions
- Such motions create long-wavelength spatial gradients that are visible in InSAR-derived velocity maps after removing other signals
- Plate motion effects can be easily accounted for using plate motion models, allowing long-wavelength deformation to be more clearly seen



## Abstract

Interferometric Synthetic Aperture Radar (InSAR) measurements are increasingly being used to measure small amplitude tectonic deformations over large spatial scales. Residual signals are often present at these scales, and are interpreted to be noise of indeterminate origin, limiting studies of long-wavelength deformation. Here, we demonstrate the impact of bulk motion by the Earth's tectonic plates on InSAR-derived velocity fields. The range-dependent incidence angle of the InSAR observations, coupled with plate velocities of centimeters per year, can induce long-wavelength spatial gradients of millimeters per year over hundreds of kilometers in InSAR-derived velocity fields. We show that, after applying corrections, including for the ionosphere and troposphere, plate motion represents the dominant source of long-wavelength secular velocity gradients in multi-year time series for several study areas. This signal can be accounted for using plate motion models, allowing improved detection of regional tectonic strain at continental scales.

## Plain Language Summary

Interferometric Synthetic Aperture Radar (InSAR) relies on repeat radar imaging to measure small motions of the Earth's surface. These motions can be used to understand a range of processes happening below the surface, from hydrology to tectonics. We show how the slow motion of Earth's tectonic plates can create a signal in InSAR data that may be confused with local tectonic signals. We also demonstrate a simple method for removing this signal, making InSAR more useful for studying very small motions over large areas of the Earth, especially in regions where we do not have good observations from other sources.

## 1 Introduction

Interferometric Synthetic Aperture Radar (InSAR) is an active imaging technique for measuring ground displacements that occur between repeat passes of an imaging platform, such as a satellite (e.g. Massonnet and Feigl (1998); Hanssen (2001); Simons and Rosen (2015)). InSAR deformation measurements are generally expressed relative to a single point, or ensemble of points, within the imaged area, usually assumed to be stable through time (e.g. Mahapatra et al. (2018)). While InSAR has been used extensively

for measuring large amplitude ( $> 1$  cm), deformation over short-wavelengths ( $< 100$  km) (e.g. Massonnet et al. (1993); Merryman Boncori (2019)), other signals present in the data challenge our ability to measure deformation at the scale of millimeters per year over hundreds of kilometers.

InSAR observations at long wavelengths are the combination of motion of the Earth’s surface, changes in the atmosphere, and measurement and processing errors. The Earth motion signals comprise the surface deformation of interest, e.g. from tectonic strain, volcanic activity or subsidence (Massonnet et al. (1993); Massonnet and Feigl (1998); Amelung et al. (1999)), along with solid Earth tides (SET) (X. Xu & Sandwell, 2020), and ocean tidal loading (Dicaprio et al., 2008). Atmospheric signals come from propagation delay through the ionosphere (Z.-W. Xu et al., 2004) and troposphere (Tarayre & Massonnet, 1996). Errors sources include the satellite orbits (Massonnet & Feigl, 1998), local oscillator drift (Marinkovic & Larsen, 2015), phase unwrapping (Biggs et al., 2007) and topography (Berardino et al., 2002).

These effects can obscure small amplitude, long-wavelength signals in InSAR due to local tectonic processes, such as surface deformation from interseismic loading (e.g. Fournier et al. (2011); Parizzi et al. (2021)). Thus, it is common to not interpret long-wavelength signals from InSAR alone, instead removing them by empirically fitting 2D polynomial functions, known as “ramps”, to the data (e.g. Fialko (2006); Jolivet et al. (2015)), or combining InSAR velocities with Global Navigation Satellite System (GNSS) measurements in order to constrain the long-wavelength deformation (e.g. Weiss et al. (2020); X. Xu et al. (2021); Neely et al. (2020); Parizzi et al. (2020)). Such approaches are limiting when we wish to measure large-scale deformation in regions of sparse GNSS coverage (Chaussard et al., 2016; Neely et al., 2020).

The quality of InSAR data and correction methods have substantially increased over the last several years. The European Space Agency’s (ESA) Sentinel-1 satellites have been regularly acquiring data for significant portions of the planet since late 2014. Sentinel-1 offers the advantages of improved orbital controls and uncertainties, reducing the noise contribution from satellite orbits (Fattahi & Amelung, 2014), as well as unrestricted data access. Split-band processing now allows for the estimation of the ionospheric signal directly from the InSAR data (Gomba et al., 2016; Fattahi, Simons, & Agram, 2017; Liang et al., 2019), and higher quality weather models have improved the correction of tropo-

spheric phase (Li et al., 2005; Doin et al., 2009; Jolivet et al., 2011). Techniques for removing the SET (X. Xu & Sandwell, 2020) and ocean tidal loading signals (Dicaprio et al., 2008; Yu et al., 2020) have also been developed, among other correction methods. After corrections, there may still be long-wavelength residuals in multi-year Sentinel-1 time series, including from the troposphere, which can contribute up to 5 mm/yr over 150 km (Parizzi et al., 2021), and orbital errors, contributing around 0.5 mm/yr over 100 km for Sentinel-1 (Fattahi & Amelung, 2014).

In this work, we focus on the contribution of coherent uniform motion of Earth’s tectonic plates to the long-wavelength component of InSAR-derived velocity fields. The satellite line-of-sight (LOS) vector varies systematically in the satellite range direction (i.e. across the satellite track). causing a changing sensitivity to ground deformation with range. Bulk motion of tectonic plates in the satellite frame of reference, coupled with this LOS variation, can create quasi-linear gradients in InSAR-derived velocity fields, resulting in ramps, predominantly in the satellite range direction. This effect has been noted before, e.g., by Bähr et al. (2012), Bähr (2013) and Parizzi et al. (2020). Here, we demonstrate that plate motion creates ramps of several millimeters per year, across the 250 km track width, in six multi-year Sentinel-1 InSAR time series. After other corrections have been applied, plate motion is the dominant long-wavelength signal in our data, and we show that this signal can be straightforwardly compensated for using plate motion models. This adjustment is not currently part of several open-source InSAR time series analysis packages (e.g Hooper et al. (2012); Agram et al. (2013); Yunjun et al. (2019); Morishita et al. (2020)), and we provide an implementation of the method in the MintPy package (Yunjun et al., 2019).

## 2 The Reference Frame of InSAR Measurements

Quantifying ground deformation using InSAR requires a precise measurement of the satellite orbit ephemerides (Fattahi & Amelung, 2014; Peter, 2021). For Sentinel-1 the orbit is measured with respect to the International Terrestrial Reference Frame (ITRF) (Peter, 2021), an Earth-centered, Earth-fixed reference frame in which there is no net rotation of the Earth’s surface (Altamimi et al., 2016). Observations of absolute ground motion relative to the satellite are therefore also in ITRF (Bähr et al., 2012; Lazecky & Hooper, 2022).

However, it is not possible for InSAR to record absolute motions due to the  $2\pi$  ambiguity in the interferometric phase (e.g. Massonnet and Feigl (1998)). Instead, displacement measurements are generally expressed relative to a reference point within the imaged region, assumed to be stationary. Velocities can then be obtained from functional fits to displacement time series, with inferred velocities also expressed relative to this point.

Selecting the reference point is not equivalent to expressing the InSAR velocities in a reference frame moving with that point (Bähr et al., 2012; Bähr, 2013). We must therefore consider how velocities in ITRF appear in the InSAR deformation field. We represent the 3D ITRF secular velocity field of the Earth’s surface as:

$$\mathbf{v}(\mathbf{x}) = \mathbf{v}_p(\mathbf{x}) + \mathbf{v}_d(\mathbf{x}). \quad (1)$$

$\mathbf{v}_p(\mathbf{x})$  is the velocity field due to the strain-free motion of the relevant rigid plate in ITRF, and  $\mathbf{v}_d(\mathbf{x})$  is the velocity due to internal deformation of the plate, for example due to tectonic, volcanic, or hydrological processes.

Defining the LOS unit vector pointing from the ground to the satellite as  $\hat{\mathbf{l}}(\mathbf{x})$ , the LOS projection of the 3D velocity field, minus the InSAR reference velocity, can be written as:

$$v_l(\mathbf{x}) = \mathbf{v}(\mathbf{x}) \cdot \hat{\mathbf{l}}(\mathbf{x}) - \mathbf{v}(\mathbf{x}') \cdot \hat{\mathbf{l}}(\mathbf{x}'), \quad (2)$$

where the reference is at point  $\mathbf{x}'$ .  $v_l(\mathbf{x})$  is the secular velocity that will be measured by the satellite, assuming all other signals and noise can be neglected.

In ITRF,  $\mathbf{v}_l(\mathbf{x})$  has a contribution from the plate motion, which we can write as:

$$\mathbf{v}_{l,p}(\mathbf{x}) = \mathbf{v}_p(\mathbf{x}) \cdot \hat{\mathbf{l}}(\mathbf{x}) - \mathbf{v}_p(\mathbf{x}') \cdot \hat{\mathbf{l}}(\mathbf{x}'). \quad (3)$$

The second term, from the reference, is constant, while the first term depends on the spatial variation of  $\mathbf{v}_p(\mathbf{x})$  and  $\hat{\mathbf{l}}(\mathbf{x})$ . The LOS vector  $\hat{\mathbf{l}}(\mathbf{x})$  can vary substantially over an image swath. For Sentinel-1, the incidence angle (the angle between the LOS and the vertical) varies approximately from  $29^\circ$  in the near range to  $46^\circ$  in the far range over the 250-km-width of the imaging swath (for data acquired in Interferometric Wideswath mode). The range-dependent variation in  $\hat{\mathbf{l}}(\mathbf{x})$  implies a changing sensitivity to components of the 3D deformation field across the track, with sensitivity to horizontal motion increasing and vertical motion decreasing as we move from near range to far range. This range-dependent sensitivity causes uniform plate motions to appear as velocity ramps in the range direction when projected into the satellite LOS (Figure 1).

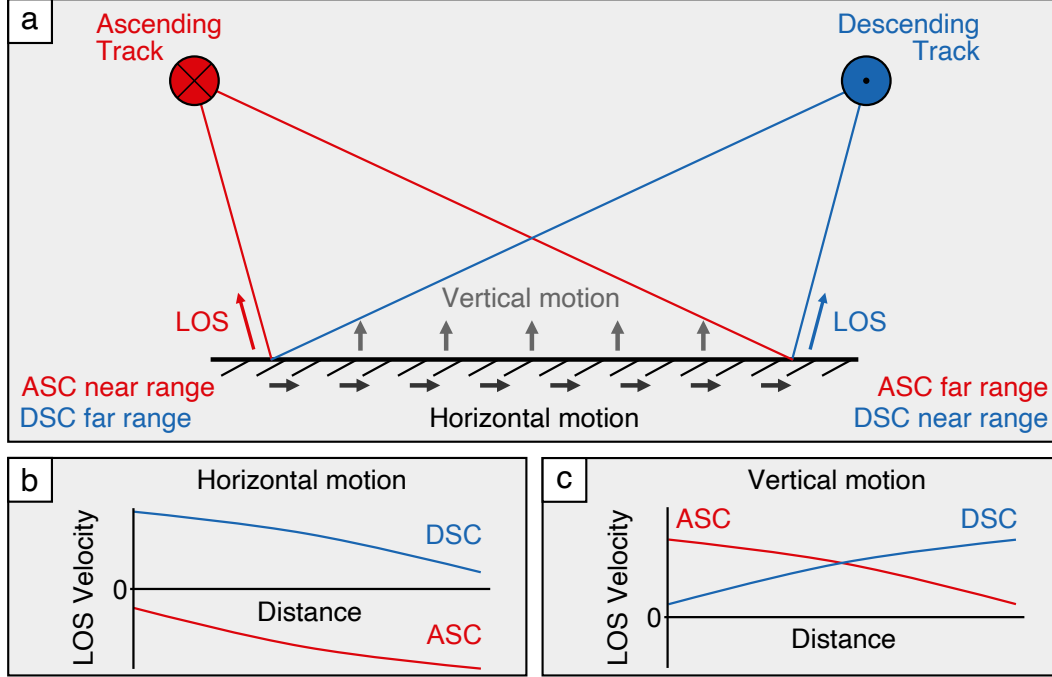


**Figure 1.** Illustration of how uniform horizontal and vertical motions result in ramps in InSAR-derived velocity measurements. **(a)** Satellite images acquired from ascending (ASC) and descending (DSC) orbital tracks, which have a varying LOS incidence angle across the track. The term “range” refers to the distance from the ground target to the satellite, with near range and far range the closest and furthest points from the satellite respectively. Red and blue arrows represent the ground-to-satellite LOS vector in the near range for ASC and DSC tracks, respectively. Grey and black arrows represent plate motion in the reference frame of the satellite. For illustration purposes we assume the ASC and DSC tracks are parallel to each other but in opposite directions, ignore Earth curvature. Figure not to scale. **(b)** Profile of the horizontal plate velocity projected into the LOS of the ASC and DSC tracks, against geographic distance along the ground. **(c)** Same as (b), except for vertical plate motion, resulting in opposite gradients in the LOS profiles. The observing geometry creates a small curvature in all profiles, which is exaggerated in the figure. For InSAR measurements, the LOS velocity is expressed relative to a point within the image, so each of these profiles would be vertically shifted to intersect with the  $x$  axis at the chosen reference point.

The plate velocity,  $\mathbf{v}_p(\mathbf{x})$ , also varies over an image swath. The motion of a rigid plate on Earth’s surface can be represented by a rotation rate about an axis, known as an Euler pole (McKenzie & Parker, 1967). Given the angular velocity of a chosen plate,  $\mathbf{\Omega}$ , we can write the velocity of any point,  $\mathbf{x}$ , on that plate as  $\mathbf{v}_p(\mathbf{x}) = \mathbf{\Omega} \times \mathbf{x}$ , where  $\times$  is the cross product. Thus, the velocity field due to rigid plate motion varies with distance from the plate’s Euler pole. This variation in  $\mathbf{v}_p(\mathbf{x})$  also contributes to the long-wavelength LOS velocity field.

Because of the effect of plate motions, InSAR velocity measurements should not generally be considered to be in a local reference frame, despite the use of a local reference point. Choosing a reference point within an InSAR image offsets InSAR velocity measurements from the LOS projection of ITRF velocities by an unknown constant (Equation 1), but does not remove the long-wavelength gradients that can be induced by plate motion (Equation 3). If ITRF plate motion is negligible when projected to the LOS, and does not vary substantially over the InSAR track, or the satellite LOS variation across the track is small, then  $\mathbf{v}_{l,p}(\mathbf{x}) \approx 0$ . Choosing a reference point that is stable with respect to the plate is then approximately equivalent to putting the InSAR velocities into the reference frame of that plate, however this should not be generally assumed.

Several authors have investigated the reference frame of InSAR observations, generally in the context of using GNSS to put InSAR measurements into a terrestrial reference frame (e.g. Mahapatra et al. (2018); Johnston et al. (2021)). The influence of plate motion on InSAR velocities has been noted by Bähr et al. (2012) and Bähr (2013), who term it the *reference frame effect*. Bähr et al. (2012) present this phenomenon in terms of a temporally increasing correction to the interferometric baseline, while Bähr (2013) notes that this can also be framed in terms of the varying satellite LOS causing differing sensitivity to plate motion (the approach taken here). Parizzi et al. (2020) used plate motion models to adjust their LOS velocity fields after merging InSAR with GNSS. Authors have also noted the impact of plate motions on SAR geolocation accuracy (Cong et al. (2012)). Our focus here is to demonstrate that plate motions can explain a significant fraction of observed residual long-wavelength surface velocities, after other corrections have been applied, and without combining InSAR data with GNSS.

### 3 Data and Methods

#### 3.1 Data Processing

We present several examples using InSAR data from the ESA’s Sentinel-1 satellites, taken from ascending (ASC) and descending (DSC) tracks covering the Makran subduction zone (Iran), the Gulf of Aqaba (at the northern end of the Red Sea), and western Australia. For each track, we process at least 5 years of data using the InSAR Scientific Computing Environment (ISCE) (Rosen et al., 2012; Fattahi, Agram, & Simons, 2017). After forming the interferogram networks, we create deformation time series using MintPy (Yunjun et al., 2019).

Before examining residual signals due to plate motion, we apply corrections for the ionosphere, troposphere, SET, and digital elevation model (DEM) error. We use split-band processing to correct for the ionosphere (Liang et al., 2019), PyAPS and the ERA5 weather model to mitigate the tropospheric delay (Jolivet et al., 2014; HERSBACH et al., 2020), the method of Fattahi and Amelung (2013) for DEM error correction and PySolid to correct for SET (Milbert, 2018; Yunjun et al., 2022). Further details of our data and processing are presented in the supporting information (Text S1, S2 and Table S1).

#### 3.2 Adjusting InSAR Measurements for Plate Motion

After all other corrections have been applied, we can then observe and account for the signal of plate motion. InSAR observations of ground motion are generally used to study regional deformation, rather than plate translations or rotations. For such purposes, a useful reference frame is one that moves with the plate in which we are trying to measure strain. Translating into this reference frame requires us to remove the signal of plate motion in the satellite’s frame of reference, i.e. ITRF (Bähr, 2013; Parizzi et al., 2020).

GNSS networks can be used to connect InSAR measurements to ITRF (e.g. Mahapatra et al. (2018); Johnston et al. (2021)), which can then be transformed into a reference frame moving with the chosen plate. In the absence of sufficient GNSS coverage, we can estimate the transformation into the plate’s frame of reference using the following steps:

1. Choose an InSAR reference point,  $\mathbf{x}'$ , that is stable with respect to the plate
2. Find the velocity field of the plate within ITRF, i.e.  $\mathbf{v}_p(\mathbf{x})$

3. Project that velocity field into the satellite LOS direction
4. Subtract the LOS velocity of the reference point,  $\mathbf{v}_{l,p}(\mathbf{x}')$ , from the projected plate velocity to compute  $\mathbf{v}_{l,p}(\mathbf{x})$ , which is then removed from the InSAR velocity map.

Note that, after these steps, InSAR-derived velocities are still expressed relative to a reference point, meaning that deformation and other signals seen at the reference point will still affect the entire scene.

We use the geodetically constrained ITRF plate motion model of Altamimi et al. (2017) to estimate the plate velocity field. For each study region, we identify our reference plate (Table S1), then use the modeled angular velocity of the plate to calculate horizontal velocities for our observation region. We then project these velocities into the LOS direction and remove them from the velocity map.

## 4 Results

### 4.1 The Importance of Removing Other Signals for Revealing Plate Motion

We expect plate motion to contribute below 8 mm/yr across the 250 km width of the Sentinel-1 tracks for our chosen regions (Figure S6), making it important to remove other signals to show what fraction of the residual velocity can be explained by plate motion. For ASC tracks in the Makran and Gulf of Aqaba, ionosphere corrections have a particularly large effect on the long-wavelength velocity signal (e.g. contributing a 25 mm/yr ramp along track 86 for the Makran, Figure 2), with DSC tracks showing substantially less ionospheric signal. ASC tracks are acquired at dusk—a period of greater ionosphere activity than dawn, when DSC tracks are acquired. This impact is still notable in C-band Sentinel-1 data, even though it suffers much less from ionospheric effects than L-band (Fattahi, Simons, & Agram, 2017; Liang et al., 2019).

We find that troposphere corrections have a less significant impact on the long-wavelength velocity signal than the ionosphere for ASC tracks, and a comparable effect for DSC tracks. Corrections for the SET have a small effect on the long-wavelength secular velocity, contributing below 0.5 mm/yr over several hundred kilometers. The range of DEM error corrections is less than  $\pm 0.5$  mm/yr in our results and has a minimal contribution to the



long-wavelength velocity field. We show the impact of the above corrections for all tracks in Figures 2 and S1-S5, and present more details in Text S2.

## 4.2 The Impact of Accounting for Plate Motion

After applying the suite of corrections we are left with residual velocity ramps in all of our tracks, predominantly in the range direction. We present the results of plate motion adjustments for several tracks in Figures 3 and 4. Our results show that accounting for plate motion removes a significant fraction of the residual velocity ramp in every case, reducing the across-track ramps from 4-7 mm/yr/track to below 1.5 mm/yr/track. For our data the plate motion signal is comparable to the troposphere in its effect on the long-wavelength velocity field.

The proximity of the Arabian plate Euler pole to the Gulf of Aqaba study area results in the plate velocity field varying appreciably within the tracks (Altamimi et al., 2017). This variation causes an additional LOS velocity ramp along the track, with an opposite direction for the ascending and descending tracks. Figures 4 (a) and (b) show how this along track gradient can be clearly seen in the data, and is well corrected for by the plate motion model. We do not see similar along-track ramps for Australia and Makran, which is consistent with the plate motion velocity field.

## 5 Discussion

Other authors have previously noted that plate motion will affect InSAR velocity measurements (e.g. Bähr et al. (2012)), however the narrower variation of the satellite LOS angle for earlier satellites, more limited data, and the presence of other significant long-wavelength signals, has made the signal difficult to isolate. The quality of recently available data and correction methods, and the wide swath of Sentinel-1, allow us to show the plate motion signal and the clear impact of accounting for it. Our results from the Gulf of Aqaba illustrate that plate rotation is an important part of the correction.

After adjusting for plate motion, remaining long-wavelength signals could be due to the incomplete removal of some signals (predominantly the troposphere (Fattahi & Amelung, 2015; Parizzi et al., 2021)), sources that we have not corrected for (e.g. ocean tidal loading (Dicaprio et al., 2008) and orbital errors (Fattahi & Amelung, 2014)), or actual strain accumulation in the lithosphere—the signal that InSAR measurements of-

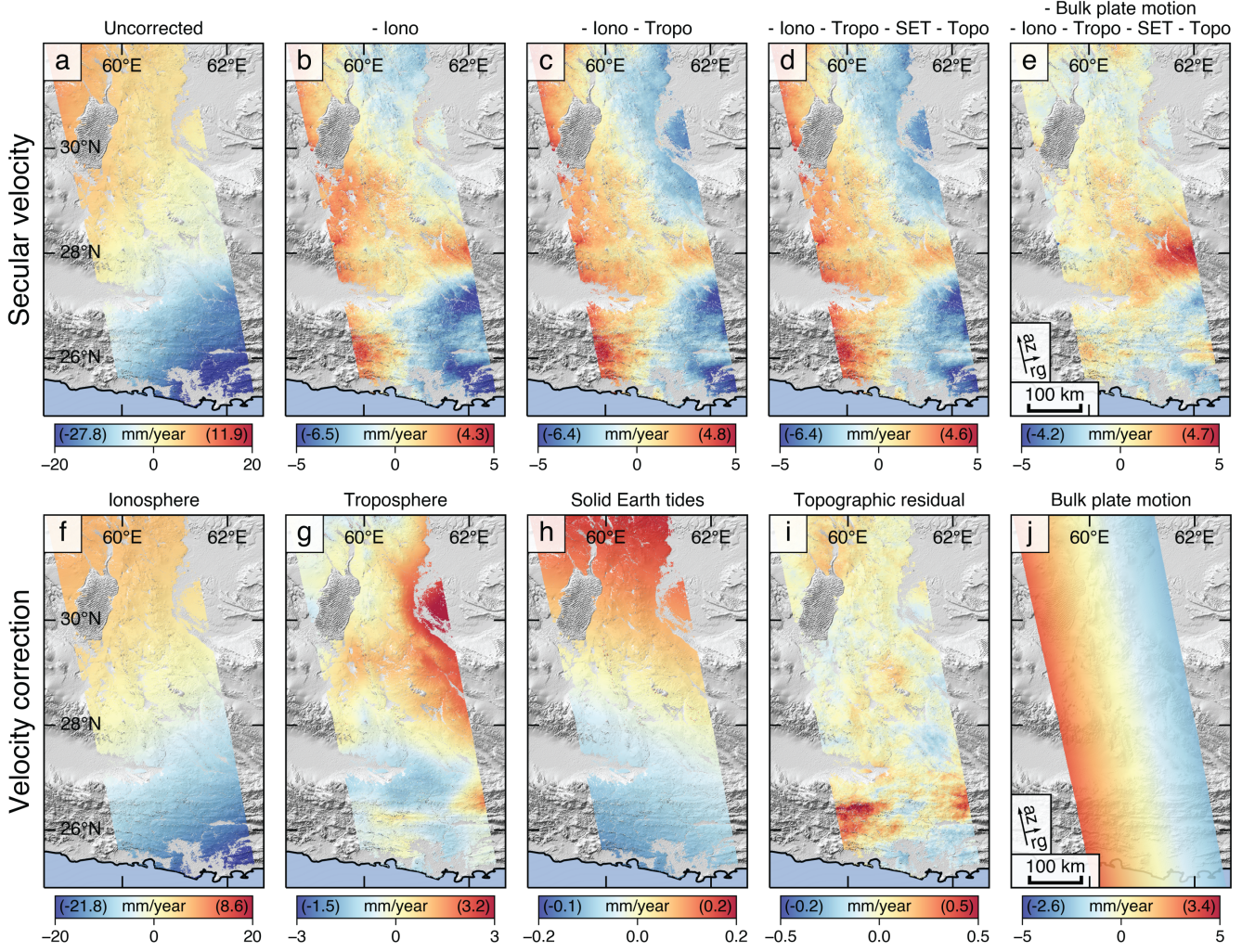


**Figure 2.** Cumulative impact of corrections on the InSAR-derived velocity field for Sentinel-1, track 86 (ASC) over the Makran subduction zone. For plotting purposes, we remove the median value from each velocity field. Positive values represent apparent motion towards the satellite. Color bars are re-scaled between plots. Numbers in parentheses within the color bars refer to the 2nd and 98th percentiles of the velocity. “az” is the azimuth direction (satellite direction of motion), and “rg” the range direction (perpendicular to the satellite direction of motion). (a) No corrections applied. (b) Estimated ionosphere removed. (c) Tropospheric model removed. (d) SET model removed and DEM error (Topo) correction applied. (e) Plate motion correction applied. The positive signal around (28 °N, 62 °E) is post-seismic deformation from the 2013 Khash earthquake (Barnhart et al., 2014). (f) Applied ionospheric correction. (g) Applied tropospheric correction. (h) Applied SET correction. (i) Applied DEM error correction. Larger signals in the south may be bias from tropospheric residuals (Fattahi & Amelung, 2014). (j) Applied plate motion correction.

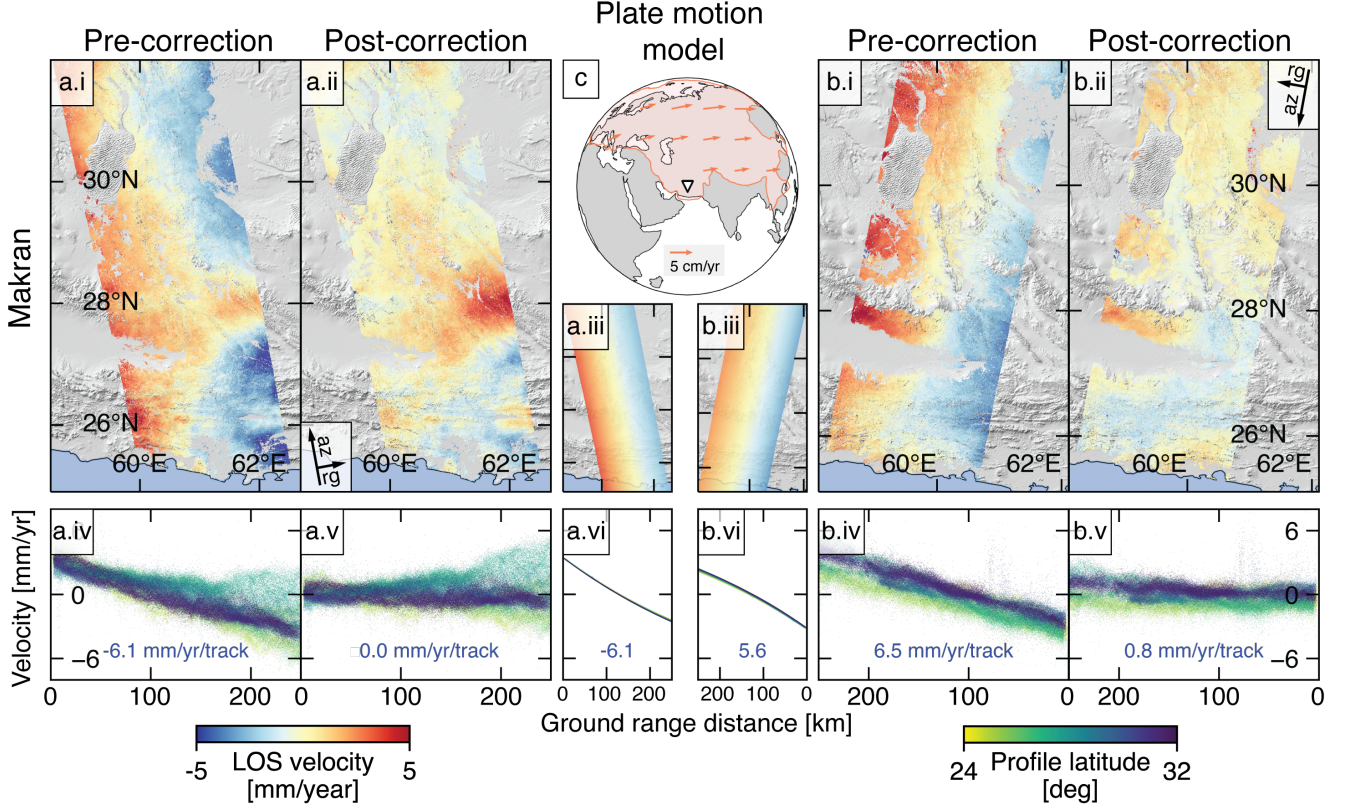


**Figure 3.** The impact of plate motion adjustments for InSAR tracks over the Makran subduction zone. For plotting purposes, we remove the median from each velocity field. **(a)** track 86 (ASC). After plate motion correction, the post-seismic signal from the 2013 Khash earthquake (Barnhart et al., 2014) can be more clearly seen in the south-east of the figure. **(b)** track 20 (DSC). **(c)** Location of tracks (a) and (b) and the velocity field of the Eurasian plate, used to correct the tracks. **(i)** Velocity before plate motion correction, but after other corrections have been applied. **(ii)** Velocity after plate motion correction. **(iii)** Applied plate motion correction. **(iv)**. Across track profile of the velocity before plate motion correction. The number below each profile is the gradient of the linear least squares fit to the profile. Note that profiles are plotted as a function of ground range, which increases with distance from the satellite. **(v)** Across track profile of the velocity after plate motion correction. **(vi)** Across track profile of the applied plate motion correction.



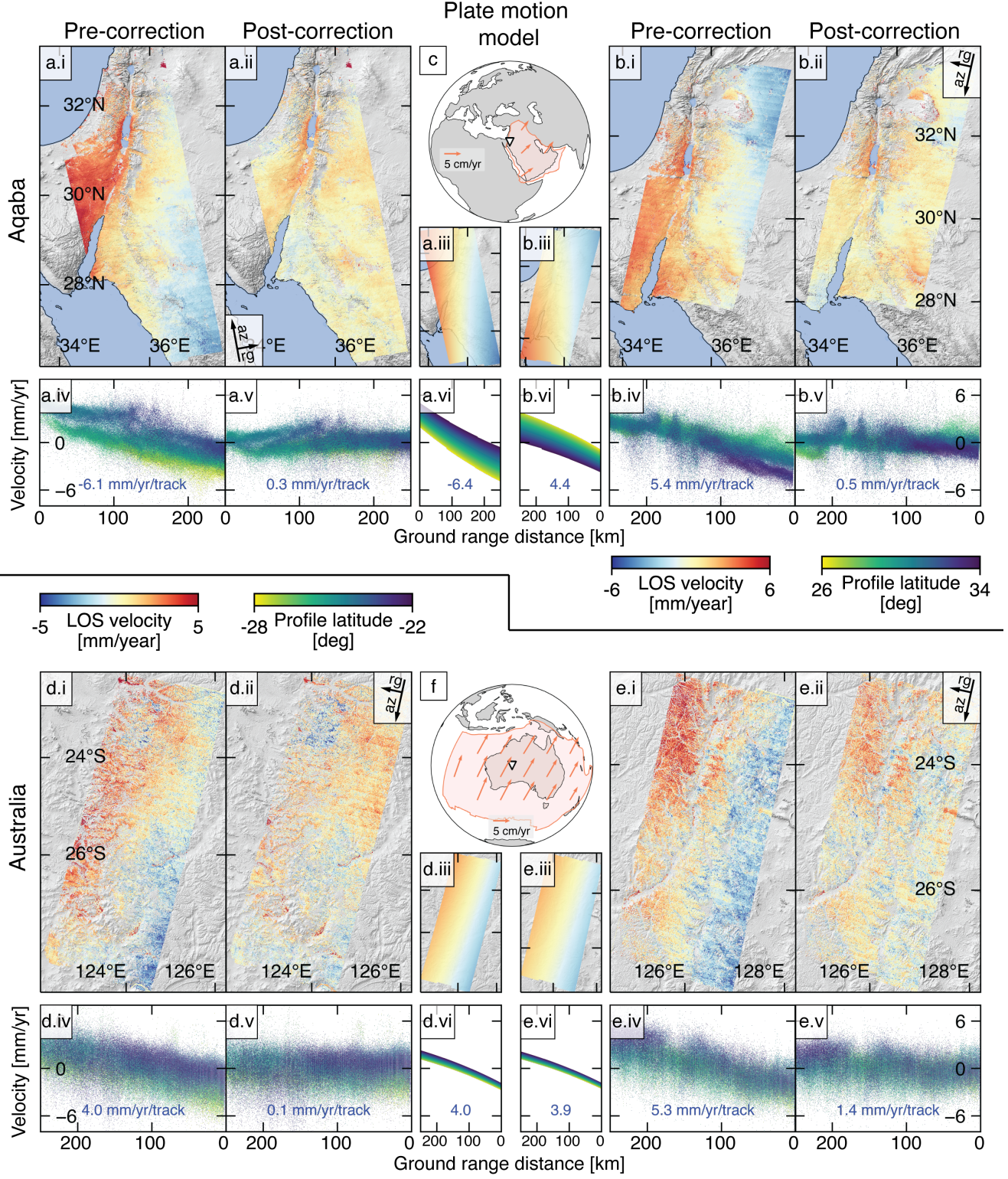


**Figure 4.** Same as Figure 3, but showing the tracks for the Gulf of Aqaba and Australia. (a) Gulf of Aqaba, track 87 (ASC). (b) Gulf of Aqaba, track 21 (DSC). (c) Location of tracks (a) and (b) and the velocity field of the Arabian plate, used to correct the tracks. (d) Australia, track 119 (DSC) (e) Australia, track 46 (DSC). (f) Location of tracks (d) and (e) and the velocity field of the Australian plate, used to correct the tracks. (i)-(vi) are as described in Figure 3.

ten target. See Text S2 for more details on the contributors to long-wavelength residuals.

Deficiencies in the plate motion model, or motion of the InSAR track reference point relative to the assumed plate, could also create long-wavelength residuals. Motion relative to the plate will be of particular importance in areas of diffuse plate boundary deformation, where it is not possible to choose a reference point that is stable with respect to the rigid plate. This could be the case for tracks covering the Makran subduction zone and the Gulf of Aqaba, both of which span plate boundary zones. In these situations, plate motion models may not fully account for the impacts of bulk motion, and using local GNSS measurements to put InSAR measurements into a local terrestrial reference frame could be necessary (Bähr, 2013).

These results emphasise the importance of accounting for the reference frame before interpreting long-wavelength InSAR-derived velocity fields. When using InSAR for studies of tectonic deformation, the most natural reference frame is one that is fixed to a stable region within the scene, so that we can interpret velocity gradients in terms of tectonic strain rather than strain-free translation and rotation. There are several situations in which failing to account for the reference frame could bias the results:

1. Combining multiple tracks to estimate 3D deformation (Fialko et al., 2001; Wright et al., 2004). In Text S4 and Figure S7 we show how plate motion can bias estimates of the 3D velocity field when we use an overlapping ascending and descending track to calculate horizontal and vertical velocities.
2. Modeling InSAR signals. If the long-wavelength signals in an InSAR velocity field are being modeled, and the model is assumed to not be rotating or translating, then a velocity ramp from plate motion may be modeled as strain accumulation and bias the results (e.g. changing the locking depth in a subduction zone model).
3. Comparisons between GNSS and InSAR. Both data sets must be in the same reference frame (Parizzi et al., 2020). If the GNSS are in a local reference frame, the InSAR and GNSS velocities will diverge at long wavelengths due to the signal of plate motion in the InSAR.

Studies which removed ramps from InSAR-derived velocities to account for orbital errors may have inadvertently removed the impact of plate motion in their observations as well, reducing the biases we outlined above.

In this work, our primary focus is on the impact of horizontal plate motions, and we have not considered the contribution of long-wavelength vertical velocities. Horizontal plate motions in ITRF are generally at the scale of centimeters per year (Altamimi et al., 2017), with long-wavelength vertical motions, for example due to post-glacial rebound, significantly smaller at millimeters per year (e.g. Riddell et al. (2020); Lau et al. (2020)). If an InSAR track is taken within a region that is experiencing constant vertical motion, this motion will also create a velocity ramp in the satellite LOS velocity field, but with ASC and DSC tracks having opposite gradients (Figure 1(c)). However, the amplitude of vertical velocities will result in smaller velocity gradients across the satellite track than those caused by horizontal motion (Text S3, Figure S6).

## 6 Conclusion

We have illustrated how InSAR velocity measurements are sensitive to tectonic plate motion in the satellite reference frame. This motion will induce ramps in the InSAR velocity fields, predominantly in the satellite range direction, of up to several millimeters per year. In all of our multi-year time series, plate motion was the dominant long-wavelength signal after ionospheric and tropospheric corrections were applied. We have presented a simple adjustment method, which uses plate motion models to remove the plate motion signal from the InSAR velocity field. This adjustment substantially reduces long-wavelength ramps in multiple InSAR tracks from three different regions of the Earth. Routinely accounting for plate motion in InSAR could reduce biases when constraining long-wavelength tectonic strain induced by local geophysical phenomena. This adjustment is likely to be particularly useful where GNSS is not available to constrain the long-wavelength deformation. The signal of plate motion in InSAR data could also be used to improve plate motion models, which may be helpful where GNSS observations are sparse but high-quality InSAR data are available.

## 7 Open Research

The Sentinel-1 data were provided by the European Space Agency and downloaded from the Alaska Satellite Facility. InSAR data were processed using the InSAR Scien-

tific Computing Environment (ISCE) (Rosen et al., 2012), available at: <https://github.com/isce-framework/isce2>. Time series analysis was performed using the MintPy software (Yunjun et al., 2019), available at: <https://github.com/insarlab/MintPy>. Our plate motion correction method is implemented in MintPy as `bulk_plate_motion.py` (for review purposes this is available at: [https://github.com/yuankailiu/MintPy/blob/GRL/mintpy/bulk\\_plate\\_motion.py](https://github.com/yuankailiu/MintPy/blob/GRL/mintpy/bulk_plate_motion.py)). Other data processing was performed using Python. Plots were produced using Matplotlib and Cartopy in Jupyter Notebooks, available at <https://zenodo.org/record/6606282>.

## Acknowledgments

Thanks to Piyush Agram and Howard Zebker for useful conversations. A portion of the work was performed at Jet Propulsion Laboratory, California Institute of Technology under contract with NASA.

## References

- Agram, P. S., Jolivet, R., Riel, B., Lin, Y. N., Simons, M., Hetland, E., . . . Lasserre, C. (2013). New Radar Interferometric Time Series Analysis Toolbox Released. *Eos, Transactions American Geophysical Union*, 94(7), 69–70. Retrieved from <http://doi.wiley.com/10.1002/2013EO070001> doi: 10.1002/2013EO070001
- Altamimi, Z., Métivier, L., & Collilieux, X. (2012). ITRF2008 plate motion model. *Journal of Geophysical Research: Solid Earth*, 117(7), 1–14. doi: 10.1029/2011JB008930
- Altamimi, Z., Métivier, L., Rebischung, P., Rouby, H., & Collilieux, X. (2017). ITRF2014 plate motion model. *Geophysical Journal International*, 209(3), 1906–1912. doi: 10.1093/gji/ggx136
- Altamimi, Z., Rebischung, P., Métivier, L., & Collilieux, X. (2016). ITRF2014: A new release of the International Terrestrial Reference Frame modeling nonlinear station motions. *Journal of Geophysical Research: Solid Earth*, 121(8), 6109–6131. Retrieved from <http://doi.wiley.com/10.1002/2016JB013098> doi: 10.1002/2016JB013098
- Amelung, F., Galloway, D. L., Bell, J. W., Zebker, H. A., & Lacznia, R. J. (1999). Sensing the ups and downs of Las Vegas: InSAR reveals structural control of



- land subsidence and aquifer-system deformation. *Geology*, 27(6), 483. Retrieved from <https://pubs.geoscienceworld.org/geology/article/27/6/483-486/207094> doi: 10.1130/0091-7613(1999)027<0483:STUADO>2.3.CO;2
- Ansari, H., De Zan, F., & Parizzi, A. (2021). Study of Systematic Bias in Measuring Surface Deformation with SAR Interferometry. *IEEE Transactions on Geoscience and Remote Sensing*, 59(2), 1285–1301. doi: 10.1109/TGRS.2020.3003421
- Bähr, H. (2013). *Orbital effects in spaceborne synthetic aperture radar interferometry* (Doctoral dissertation). doi: 10.5445/KSP/1000037166
- Bähr, H., Samiei-Esfahany, S., & Hanssen, R. F. (2012). On The Effect Of Reference Frame Motion On InSAR Deformation Estimates. *Proceedings of Fringe 2011*.
- Barnhart, W. D., Hayes, G. P., Samsonov, S. V., Fielding, E. J., & Seidman, L. E. (2014). Breaking the oceanic lithosphere of a subducting slab: The 2013 Khash, Iran earthquake. *Geophysical Research Letters*, 41(1), 32–36. doi: 10.1002/2013GL058096
- Bekaert, D., Walters, R., Wright, T., Hooper, A., & Parker, D. (2015). Statistical comparison of InSAR tropospheric correction techniques. *Remote Sensing of Environment*, 170, 40–47. Retrieved from <https://linkinghub.elsevier.com/retrieve/pii/S0034425715301231> doi: 10.1016/j.rse.2015.08.035
- Berardino, P., Fornaro, G., Lanari, R., & Sansosti, E. (2002). A new algorithm for surface deformation monitoring based on small baseline differential SAR interferograms. *IEEE Transactions on Geoscience and Remote Sensing*, 40(11), 2375–2383. Retrieved from <http://ieeexplore.ieee.org/document/1166596/> doi: 10.1109/TGRS.2002.803792
- Biggs, J., Wright, T., Lu, Z., & Parsons, B. (2007). Multi-interferogram method for measuring interseismic deformation: Denali Fault, Alaska. *Geophysical Journal International*, 170(3), 1165–1179. doi: 10.1111/j.1365-246X.2007.03415.x
- Chaussard, E., Johnson, C. W., Fattahi, H., & Bürgmann, R. (2016). Potential and limits of InSAR to characterize interseismic deformation independently of GPS data: Application to the southern San Andreas Fault system. *Geochemistry, Geophysics, Geosystems*, 17(3), 1214–1229. Retrieved from <https://onlinelibrary.wiley.com/doi/10.1002/2015GC006246> doi: 10.1002/2015GC006246



- 373 Chen, C. W., & Zebker, H. A. (2002). Phase unwrapping for large SAR interfero-  
 374 grams: Statistical segmentation and generalized network models. *IEEE Trans-*  
 375 *actions on Geoscience and Remote Sensing*, 40(8), 1709–1719. doi: 10.1109/  
 376 TGRS.2002.802453
- 377 Cong, X., Balss, U., Eineder, M., & Fritz, T. (2012). Imaging Geodesy—Centimeter-  
 378 Level Ranging Accuracy With TerraSAR-X: An Update. *IEEE Geoscience and*  
 379 *Remote Sensing Letters*, 9(5), 948–952. Retrieved from [http://ieeexplore](http://ieeexplore.ieee.org/document/6170871/)  
 380 [.ieee.org/document/6170871/](http://ieeexplore.ieee.org/document/6170871/) doi: 10.1109/LGRS.2012.2187042
- 381 De Zan, F., Parizzi, A., Prats-Iraola, P., & López-Dekker, P. (2014). A SAR interfer-  
 382 ometric model for soil moisture. *IEEE Transactions on Geoscience and Remote*  
 383 *Sensing*, 52(1), 418–425. doi: 10.1109/TGRS.2013.2241069
- 384 Dicaprio, C. J., Simons, M., Kenner, S. J., & Williams, C. A. (2008). Post-seismic  
 385 reloading and temporal clustering on a single fault. *Geophysical Journal Inter-*  
 386 *national*, 172(2), 581–592. doi: 10.1111/j.1365-246X.2007.03622.x
- 387 Doin, M. P., Lasserre, C., Peltzer, G., Cavalié, O., & Doubre, C. (2009). Correc-  
 388 tions of stratified tropospheric delays in SAR interferometry: Validation with  
 389 global atmospheric models. *Journal of Applied Geophysics*, 69(1), 35–50. Re-  
 390 trieved from <http://dx.doi.org/10.1016/j.jappgeo.2009.03.010> doi:  
 391 10.1016/j.jappgeo.2009.03.010
- 392 Emardson, T. R., Simons, M., & Webb, F. H. (2003). Neutral atmospheric delay  
 393 in interferometric synthetic aperture radar applications: Statistical descrip-  
 394 tion and mitigation. *Journal of Geophysical Research: Solid Earth*, 108(B5),  
 395 1–8. Retrieved from <http://doi.wiley.com/10.1029/2002JB001781> doi:  
 396 10.1029/2002JB001781
- 397 Fattahi, H., Agram, P., & Simons, M. (2017). A Network-Based Enhanced  
 398 Spectral Diversity Approach for TOPS Time-Series Analysis. *IEEE*  
 399 *Transactions on Geoscience and Remote Sensing*, 55(2), 777–786. Re-  
 400 trieved from <http://ieeexplore.ieee.org/document/7637021/> doi:  
 401 10.1109/TGRS.2016.2614925
- 402 Fattahi, H., & Amelung, F. (2013). DEM Error Correction in InSAR Time Series.  
 403 *Geoscience and Remote Sensing, IEEE Transactions on*, 51(7), 4249–4259.  
 404 Retrieved from <http://ieeexplore.ieee.org/document/6423275/> doi:  
 405 10.1109/TGRS.2012.2227761

- 406 Fattahi, H., & Amelung, F. (2014). InSAR uncertainty due to orbital errors. *Geo-*  
 407 *physical Journal International*, 199(1), 549–560. doi: 10.1093/gji/ggu276
- 408 Fattahi, H., & Amelung, F. (2015). InSAR bias and uncertainty due to the system-  
 409 atic and stochastic tropospheric delay. *Journal of Geophysical Research: Solid*  
 410 *Earth*, 120(12), 8758–8773. Retrieved from [https://onlinelibrary.wiley](https://onlinelibrary.wiley.com/doi/abs/10.1002/2015JB012419)  
 411 [.com/doi/abs/10.1002/2015JB012419](https://onlinelibrary.wiley.com/doi/abs/10.1002/2015JB012419) doi: 10.1002/2015JB012419
- 412 Fattahi, H., Simons, M., & Agram, P. (2017). InSAR Time-Series Estimation  
 413 of the Ionospheric Phase Delay: An Extension of the Split Range-Spectrum  
 414 Technique. *IEEE Transactions on Geoscience and Remote Sensing*, 55(10),  
 415 5984–5996. doi: 10.1109/TGRS.2017.2718566
- 416 Fialko, Y. (2006). Interseismic strain accumulation and the earthquake potential on  
 417 the southern San Andreas fault system. *Nature*, 441(7096), 968–971. doi: 10  
 418 .1038/nature04797
- 419 Fialko, Y., Simons, M., & Agnew, D. (2001). The complete (3-D) surface displace-  
 420 ment field in the epicentral area of the 1999 Mw 7.1 Hector Mine earthquake,  
 421 California, from space geodetic observations. *Geophysical Research Letters*,  
 422 28(16), 3063–3066. doi: 10.1029/2001GL013174
- 423 Fournier, T., Pritchard, M. E., & Finnegan, N. (2011). Accounting for Atmo-  
 424 spheric Delays in InSAR Data in a Search for Long-Wavelength Deformation  
 425 in South America. *IEEE Transactions on Geoscience and Remote Sensing*,  
 426 49(10), 3856–3867. Retrieved from [http://ieeexplore.ieee.org/document/](http://ieeexplore.ieee.org/document/5771553/)  
 427 [5771553/](http://ieeexplore.ieee.org/document/5771553/) doi: 10.1109/TGRS.2011.2139217
- 428 Gomba, G., Parizzi, A., De Zan, F., Eineder, M., & Bamler, R. (2016). Toward  
 429 operational compensation of ionospheric effects in SAR interferograms: The  
 430 split-spectrum method. *IEEE Transactions on Geoscience and Remote Sens-*  
 431 *ing*, 54(3), 1446–1461. doi: 10.1109/TGRS.2015.2481079
- 432 Hanssen, R. F. (2001). *Radar Interferometry: Data Interpretation and Error Anal-*  
 433 *ysis* (Vol. 2). Dordrecht: Springer Netherlands. Retrieved from [http://link](http://link.springer.com/10.1007/0-306-47633-9)  
 434 [.springer.com/10.1007/0-306-47633-9](http://link.springer.com/10.1007/0-306-47633-9) doi: 10.1007/0-306-47633-9
- 435 Hersbach, H., Bell, B., Berrisford, P., Hirahara, S., Horányi, A., Muñoz-Sabater,  
 436 J., ... Thépaut, J. (2020). The ERA5 global reanalysis. *Quarterly Jour-*  
 437 *nal of the Royal Meteorological Society*, 146(730), 1999–2049. Retrieved  
 438 from <https://onlinelibrary.wiley.com/doi/10.1002/qj.3803> doi:

- 439 10.1002/qj.3803
- 440 Hooper, A., Bekaert, D., Spaans, K., & Arikan, M. (2012). Recent advances in SAR  
441 interferometry time series analysis for measuring crustal deformation. *Tectono-*  
442 *physics*, 514-517, 1–13. doi: 10.1016/j.tecto.2011.10.013
- 443 Johnston, P. J., Filmer, M. S., & Fuhrmann, T. (2021). Evaluation of methods  
444 for connecting InSAR to a terrestrial reference frame in the Latrobe Valley,  
445 Australia. *Journal of Geodesy*, 95(10). Retrieved from [https://doi.org/](https://doi.org/10.1007/s00190-021-01560-2)  
446 10.1007/s00190-021-01560-2 doi: 10.1007/s00190-021-01560-2
- 447 Jolivet, R., Agram, P. S., Lin, N. Y., Simons, M., Doin, M.-p., Peltzer, G., & Li, Z.  
448 (2014). Improving InSAR geodesy using Global Atmospheric Models. *Jour-*  
449 *nal of Geophysical Research: Solid Earth*, 119(3), 2324–2341. Retrieved from  
450 <https://onlinelibrary.wiley.com/doi/abs/10.1002/2013JB010588> doi:  
451 10.1002/2013JB010588
- 452 Jolivet, R., Grandin, R., Lasserre, C., Doin, M. P., & Peltzer, G. (2011). Sys-  
453 tematic InSAR tropospheric phase delay corrections from global meteorolo-  
454 gical reanalysis data. *Geophysical Research Letters*, 38(17), 1–6. doi:  
455 10.1029/2011GL048757
- 456 Jolivet, R., Simons, M., Agram, P. S., Duputel, Z., & Shen, Z.-K. (2015). Aseismic  
457 slip and seismogenic coupling along the central San Andreas Fault. *Geophysical*  
458 *Research Letters*, 42(2), 297–306. Retrieved from [http://doi.wiley.com/10](http://doi.wiley.com/10.1002/2014GL062222)  
459 .1002/2014GL062222 doi: 10.1002/2014GL062222
- 460 Lau, N., Borsa, A. A., & Becker, T. W. (2020). Present-Day Crustal Vertical Veloc-  
461 ity Field for the Contiguous United States. *Journal of Geophysical Research:*  
462 *Solid Earth*, 125(10). Retrieved from [https://onlinelibrary.wiley.com/](https://onlinelibrary.wiley.com/doi/10.1029/2020JB020066)  
463 doi/10.1029/2020JB020066 doi: 10.1029/2020JB020066
- 464 Lazecky, M., & Hooper, A. (2022). InSAR-derived horizontal velocities in  
465 a global reference frame. *ESSOAr (preprint)*, 1–14. Retrieved from  
466 <https://www.essoar.org/doi/abs/10.1002/essoar.10511058.1> doi:  
467 <https://doi.org/10.1002/essoar.10511058.1>
- 468 Li, Z., Muller, J. P., Cross, P., & Fielding, E. J. (2005). Interferometric synthetic  
469 aperture radar (InSAR) atmospheric correction: GPS, Moderate Resolution  
470 Imaging Spectroradiometer (MODIS), and InSAR integration. *Journal of*  
471 *Geophysical Research: Solid Earth*, 110(3), 1–10. doi: 10.1029/2004JB003446

- 472 Li, Z., Wright, T., Hooper, A., Crippa, P., Gonzalez, P., Walters, R., ... Par-  
473 sons, B. (2016). Towards InSAR everywhere, all the time, with Sentinel-  
474 1. *International Archives of the Photogrammetry, Remote Sensing and*  
475 *Spatial Information Sciences - ISPRS Archives*, 41(July), 763–766. doi:  
476 10.5194/isprsarchives-XLI-B4-763-2016
- 477 Liang, C., Agram, P., Simons, M., & Fielding, E. J. (2019). Ionospheric Correction  
478 of InSAR Time Series Analysis of C-band Sentinel-1 TOPS Data. *IEEE Trans-*  
479 *actions on Geoscience and Remote Sensing*, 57(9), 6755–6773. doi: 10.1109/  
480 tgrs.2019.2908494
- 481 Mahapatra, P., der Marel, H. v., van Leijen, F., Samiei-Esfahany, S., Klees,  
482 R., & Hanssen, R. (2018). InSAR datum connection using GNSS-  
483 augmented radar transponders. *Journal of Geodesy*, 92(1), 21–32. doi:  
484 10.1007/s00190-017-1041-y
- 485 Marinkovic, P., & Larsen, Y. (2015). On Resolving the Local Oscillator Drift In-  
486 duced Phase Ramps in ASAR and ERS1/2 Interferometric Data—The Final  
487 Solution. *Fringe 2015 Workshop (ESA SP - 731)*(1), 20.
- 488 Massonnet, D., & Feigl, K. L. (1998). Radar interferometry and its application to  
489 changes in the Earth’s surface. *Reviews of Geophysics*, 36(4), 441. Retrieved  
490 from <http://doi.wiley.com/10.1029/97RG03139> doi: 10.1029/97RG03139
- 491 Massonnet, D., Rossi, M., Carmona, C., Adragna, F., Peltzer, G., Feigl, K., &  
492 Rabaute, T. (1993). The displacement field of the Landers earthquake  
493 mapped by radar interferometry. *Nature*, 364(6433), 138–142. Retrieved  
494 from <http://www.nature.com/articles/364138a0> doi: 10.1038/364138a0
- 495 McKenzie, D. P., & Parker, R. L. (1967). The North Pacific: an Example of Tecton-  
496 ics on a Sphere. *Nature*, 216(5122), 1276–1280. Retrieved from [https://www](https://www.nature.com/articles/2161276a0)  
497 [.nature.com/articles/2161276a0](https://www.nature.com/articles/2161276a0) doi: 10.1038/2161276a0
- 498 Merryman Boncori, J. P. (2019). Measuring Coseismic Deformation With Space-  
499 borne Synthetic Aperture Radar: A Review. *Frontiers in Earth Science*,  
500 7(February), 1–20. doi: 10.3389/feart.2019.00016
- 501 Milbert, D. (2018). *solid: Solid Earth Tide*. Retrieved from [https://geodesyworld](https://geodesyworld.github.io/SOFTS/solid.htm)  
502 [.github.io/SOFTS/solid.htm](https://geodesyworld.github.io/SOFTS/solid.htm)
- 503 Morishita, Y., Lazecky, M., Wright, T., Weiss, J., Elliott, J., & Hooper, A. (2020).  
504 LiCSBAS: An Open-Source InSAR Time Series Analysis Package Integrated

- with the LiCSAR Automated Sentinel-1 InSAR Processor. *Remote Sensing*,  
*12*(3), 424. Retrieved from <https://www.mdpi.com/2072-4292/12/3/424>  
doi: 10.3390/rs12030424
- Neely, W. R., Borsa, A. A., & Silverii, F. (2020). GInSAR: A cGPS Correction for  
Enhanced InSAR Time Series. *IEEE Transactions on Geoscience and Remote  
Sensing*, *58*(1), 136–146. Retrieved from [https://ieeexplore.ieee.org/  
document/8839742/](https://ieeexplore.ieee.org/document/8839742/) doi: 10.1109/TGRS.2019.2934118
- Parizzi, A., Brcic, R., & De Zan, F. (2021). InSAR Performance for Large-Scale De-  
formation Measurement. *IEEE Transactions on Geoscience and Remote Sens-  
ing*, *59*(10), 8510–8520. doi: 10.1109/TGRS.2020.3039006
- Parizzi, A., Gonzalez, F. R., & Brcic, R. (2020). A covariance-based approach to  
merging InSAR and GNSS displacement rate measurements. *Remote Sensing*,  
*12*(2). doi: 10.3390/rs12020300
- Peter, H. (2021). *Copernicus POD Product Handbook: Copernicus Sentinel-1, -2  
and -3 Precise Orbit Determination Service (CPOD)* (Tech. Rep.). GMV.  
Retrieved from [https://sentinel.esa.int/documents/247904/4599719/  
Copernicus-POD-Product-Handbook.pdf](https://sentinel.esa.int/documents/247904/4599719/Copernicus-POD-Product-Handbook.pdf)
- Petit, G., & Luzum, B. (2010). *IERS Conventions (IERS Technical Note No. 36)*.  
Frankfurt, Germany. Retrieved from <http://www.iers.org/TN36/>
- Riddell, A. R., King, M. A., & Watson, C. S. (2020). Present-Day Vertical Land Mo-  
tion of Australia From GPS Observations and Geophysical Models. *Journal of  
Geophysical Research: Solid Earth*, *125*(2). doi: 10.1029/2019JB018034
- Rosen, P. A., Gurrola, E., Sacco, G. F., & Zebker, H. (2012). The InSAR scientific  
computing environment. In *Proceedings of the european conference on synthetic  
aperture radar, eusar* (Vol. 2012-April, pp. 730–733).
- Simons, M., & Rosen, P. (2015). Interferometric Synthetic Aperture Radar Geodesy.  
In *Treatise on geophysics* (Vol. 3, pp. 339–385). Elsevier. Retrieved from  
<https://linkinghub.elsevier.com/retrieve/pii/B9780444538024000610>  
doi: 10.1016/B978-0-444-53802-4.00061-0
- Tarayre, H., & Massonnet, D. (1996). Atmospheric Propagation heterogeneities  
revealed by ERS-1 interferometry. *Geophysical Research Letters*, *23*(9), 989–  
992. Retrieved from <http://doi.wiley.com/10.1029/96GL00622> doi: 10  
.1029/96GL00622

- Weiss, J. R., Walters, R. J., Morishita, Y., Wright, T. J., Lazecky, M., Wang, H., . . .  
 Parsons, B. (2020). High-Resolution Surface Velocities and Strain for Anatolia  
 From Sentinel-1 InSAR and GNSS Data. *Geophysical Research Letters*, 47(17).  
 doi: 10.1029/2020GL087376
- Wright, T. J., Parsons, B. E., & Lu, Z. (2004). Toward mapping surface deformation  
 in three dimensions using InSAR. *Geophysical Research Letters*, 31(1), 1–  
 5. doi: 10.1029/2003GL018827
- Xu, X., & Sandwell, D. T. (2020). Toward Absolute Phase Change Recovery  
 with InSAR: Correcting for Earth Tides and Phase Unwrapping Ambiguities.  
*IEEE Transactions on Geoscience and Remote Sensing*, 58(1), 726–733. doi:  
 10.1109/TGRS.2019.2940207
- Xu, X., Sandwell, D. T., Klein, E., & Bock, Y. (2021). Integrated Sentinel-1 InSAR  
 and GNSS Time-Series Along the San Andreas Fault System. *Journal of Geo-  
 physical Research: Solid Earth*, 126(11), 1–14. doi: 10.1029/2021JB022579
- Xu, Z.-W., Wu, J., & Wu, Z.-S. (2004). A survey of ionospheric effects on space-  
 based radar. *Waves in Random Media*, 14(2), S189-S273. Retrieved from  
<http://www.tandfonline.com/doi/abs/10.1088/0959-7174/14/2/008> doi:  
 10.1088/0959-7174/14/2/008
- Yu, C., Penna, N. T., & Li, Z. (2020). Ocean Tide Loading Effects on InSAR Ob-  
 servations Over Wide Regions. *Geophysical Research Letters*, 47(15). doi: 10  
 .1029/2020GL088184
- Yunjun, Z., Fattahi, H., & Amelung, F. (2019). Small baseline InSAR time se-  
 ries analysis: Unwrapping error correction and noise reduction. *Computers and  
 Geosciences*, 133(May), 104331. Retrieved from [https://doi.org/10.1016/j](https://doi.org/10.1016/j.cageo.2019.104331)  
[.cageo.2019.104331](https://doi.org/10.1016/j.cageo.2019.104331) doi: 10.1016/j.cageo.2019.104331
- Yunjun, Z., Fattahi, H., Pi, X., Rosen, P., Simons, M., Agram, P., & Aoki, Y.  
 (2022). Range Geolocation Accuracy of C/L-band SAR and its Implications  
 for Operational Stack Coregistration. *IEEE Transactions on Geoscience and  
 Remote Sensing*, 2892(c), 1–1. Retrieved from [https://ieeexplore.ieee](https://ieeexplore.ieee.org/document/9759304/)  
[.org/document/9759304/](https://ieeexplore.ieee.org/document/9759304/) doi: 10.1109/TGRS.2022.3168509
- Zebker, H. A., & Villasenor, J. (1992). Decorrelation in interferometric radar echoes.  
*IEEE Transactions on Geoscience and Remote Sensing*, 30(5), 950–959. doi:  
 10.1109/36.175330

571 Zheng, Y., Fattahi, H., Agram, P., Simons, M., & Rosen, P. (2022). On  
572 Closure Phase and Systematic Bias in Multilooked SAR Interferometry.  
573 *IEEE Transactions on Geoscience and Remote Sensing*, 60, 1–11. Re-  
574 trieved from <https://ieeexplore.ieee.org/document/9758802/> doi:  
575 10.1109/TGRS.2022.3167648

# Supporting Information for: “The Impact of Plate Motions on Long-Wavelength InSAR-Derived Velocity Field”

Oliver L. Stephenson<sup>1</sup>, Yuan-Kai Liu<sup>1</sup>, Zhang Yunjun<sup>1</sup>, Mark Simons<sup>1</sup>,  
and Paul Rosen<sup>2</sup>

<sup>1</sup>Seismological Laboratory, Division of Geological and Planetary Sciences,

California Institute of Technology, Pasadena, CA 91125, USA.

<sup>2</sup>Jet Propulsion Laboratory, California Institute of Technology, Pasadena, CA 91109, USA.

## Contents of this File

1. Text S1 to S4
2. Table S1
3. Figures S1 to S7

## Introduction

Here, we present more details on the SAR data sources (Table S1) and processing steps (Text S1). In Text S2 we give further details on the corrections that we apply to our data and the possible sources of residual signals after these corrections are applied. In Figures S1-S5 we present the velocity corrections for all tracks other than Makran track

---



86, which is shown in the main text (Figure 2). In Text S3 we provide further information on how bulk vertical and horizontal motions impact InSAR velocity fields, and in Figure S6 we present a figure that can be used to estimate the scale of velocity ramp for ascending (ASC) and descending (DSC) tracks for a given plate velocity. In the Discussion we stated that plate motion could bias calculations of 3D velocities from multiple overlapping InSAR tracks, which we illustrate in Text S4 and Figure S7.

**Text S1: InSAR Processing Details**

We download Sentinel-1 Single Look Complex (SLC) data from the Alaska Satellite Facility. We process our data using the InSAR Scientific Computing Environment (Rosen et al. (2012), and see <https://github.com/isce-framework/isce2>). For the Makran data (tracks 86 and 20), we use the topsApp processing chain, where each interferometric pair is processed separately. Other tracks are processed using topsStack, which coregisters all SLCs to a single reference image at the start of the processing. topsStack therefore avoids the need to repeat the coregistration for every interferometric pair, reducing computational expense compared to topsApp.

Each acquisition is used to form interferograms with the next three SLCs. We use satellite orbits from the Copernicus Precise Orbit Determination service and digital elevation models from the Shuttle Radar Topography Mission to remove the phase contribution from the viewing geometry. To correct for azimuth misregistration we apply enhanced spectral diversity (ESD) (De Zan et al., 2014) for each pair. When processing data using topsStack, we estimate azimuth misregistration for each date in a network sense based on ESD results for each pair (Fattahi, Agram, & Simons, 2017), but do not use the network approach for topsApp. The different approaches are unlikely to have a significantly different impact on the long wavelength velocity field from long time series. Two dimensional phase unwrapping is performed using the SNAPHU algorithm for each interferogram (Chen & Zebker, 2002).

We use the range split-spectrum method of Liang et al. (2019) to estimate the ionospheric phase screen in each interferogram. For topsStack data, the ionospheric phase

is estimated for each interferogram, then for each date by network inversion (Fattahi, Simons, & Agram, 2017). The ionosphere correction is then applied in the time series domain. For topsApp data, the ionospheric phase screen is estimated and removed before final phase unwrapping. As long as we remove interferograms where there are clear unwrapping errors in the ionosphere, we expect the difference between these approaches to be insignificant.

We calculate InSAR time series from the interferometric network using the SBAS methodology (Berardino et al., 2002), implemented in MintPy (Yunjun et al., 2019). The secular velocity is obtained from a linear, least squares fit to the time series. We use the PyAPS software package to apply corrections for the troposphere with ERA-5 weather models (Jolivet et al., 2011, 2014). Solid Earth tides removal is performed using PySolid (Milbert, 2018; Yunjun et al., 2022), and the Digital Elevation Model (DEM) error is estimated from the correlation between the residual time series and perpendicular baseline, as described in Fattahi and Amelung (2013). All of the above corrections are applied to the deformation time series. We apply the plate motion adjustment in the velocity domain. As we are performing linear least-squares fits to the time series, the plate motion correction could be straightforwardly applied to the time series (assuming a constant plate rate) with identical results. All other corrections could similarly be applied either in the velocity domain or the time series domain and result in the same final velocity, assuming that we obtain the velocities from a linear fit to the time series.

For the Makran and Aqaba data sets we mask out unreliable data based on the union of connected component masks from every interferogram (i.e. areas identified as unreliably

unwrapped by the SNAPHU algorithm (Chen & Zebker, 2002)). This is a conservative approach to masking that removes a large amount of the data, but allows us to focus on long-wavelength features. The lower coherence for our Australian tracks means that the connected component mask removes too much data to view the spatial velocity pattern, so we instead mask out points with an average spatial coherence below 0.82. This less conservative masking strategy leads us to include noisier data, possibly biasing our estimation of the across track ramp.

### **Text S2: Further Details on InSAR Corrections and Residuals**

To illustrate the influence of the corrections on the final secular velocity, we perform a linear, least squares fit to the time series of each of the applied corrections (these fits are shown in the second row of Figures 2 and S1-S5). While we fit a linear velocity term for the figures to show how the corrections affect the measured secular velocity, we do not expect these corrections to have a linear variation in time. As these corrections are not perfect, and we have not accounted for all potential contributors to our velocity fields, we also need to consider what other residuals may remain in our time series. Of particular interest is the extent to which the velocity ramps before plate motion correction can be attributed to sources other than plate motion. Below, we present more details on these corrections and the residuals that may remain in our data.

The strength of ionospheric signals is controlled by the density of charged particles in the ionosphere (Gomba et al., 2016). Ionization is mainly due to solar radiation, meaning the ionospheric signal depends on factors such as the time of day, the geomagnetic latitude, and the approximately 11-year solar cycle (Liang et al., 2019). Sentinel-1 ascending

tracks are acquired at dusk (around 6 pm local solar time), and suffer from much stronger ionospheric impacts than the Sentinel-1 descending tracks which are acquired at dawn (around 6 am local solar time). The most recent peak of solar activity occurred in April 2014, decreasing to a minimum in December 2019, meaning that data earlier in our time series (which start in late 2014 for Aqaba and Makran) have much stronger ionospheric effects than later dates. This long-term variation in the ionosphere means that we cannot average-out the ionospheric signal by fitting to several years of data, making the ionosphere the most significant correction to the secular velocity for the ascending tracks we study.

Ionospheric corrections clearly substantially reduce long-wavelength velocity ramps for the ascending tracks we present here, but it is hard to quantify what residual ionospheric signals may be left without comparing to external data. Liang et al. (2018) compared the long-wavelength signal with GNSS velocities after ionosphere correction using the split-spectrum method. They found good agreement between the long-wavelength InSAR and GNSS velocities, suggesting that residual ionosphere was not having a significant impact on the long-wavelength InSAR signals after correction.

Errors in the ionosphere estimation can be introduced by unwrapping errors in the sub-band interferograms (Gomba et al., 2016; Liang et al., 2019) and before time series processing we examine the ionospheric phase estimates and remove those that have obvious unwrapping errors. Unwrapping the sub-band interferograms requires strong filtering (Liang et al., 2019), meaning that the split-spectrum method is not able to capture short-wavelength variations in the ionospheric signal. We observe the strength of the calculated long-wavelength ionospheric signal to vary with solar activity, which declined from a

peak in April 2014 to a minimum in December 2019, and we would expect the short wavelength ionosphere to follow the same pattern. If we have a substantial component of short wavelength ionospheric noise, this might then show up as larger residuals in the time series for the earlier dates (2014-15) compared to dates in late 2019. To test this, we first fit and remove from every pixel a functional form (a linear term plus the amplitude and phase of annual and semi-annual sinusoids), then calculate the root mean square (RMS) of the residuals for every acquisition. The primary variation in the residual RMS is seasonal (e.g. varying between about 10 mm and 45 mm for track 86 (ASC) in the Makran), likely due to incompletely removed tropospheric delays. There is not a strong trend in the RMS over longer timescales, suggesting the short wavelength ionosphere remaining in our data is not having a substantial effect, particularly compared with residual troposphere.

The geometry of the Sentinel-1 bursts can result in ionospheric phase discontinuities at the burst boundaries (see Section III.C in Liang et al. (2019)). The topsApp code is able to compute and remove these discontinuities as part of the ionosphere estimation. The removal of burst discontinuities due to the ionosphere can be most clearly seen in the ladder-like pattern of the velocity in Figure S1(f), which is the calculated ionospheric signal removed from S1(a). Here, the ionosphere is contributing ramps of up to 0.5 mm/yr over the 20 km along-track width of the bursts, with sharp discontinuities of up to 0.5 mm/yr at the burst boundaries. These ramps and discontinuities are removed by the ionosphere correction. The burst ramps and discontinuities are also present in the ionosphere estimation of the ascending track (Figure 2(f)), which is also performed

using topsApp, but cannot be seen in the figure due to the wider dynamic range of the ionosphere.

The topsStack code is not yet able to take account of the burst geometry when computing the ionospheric phase screen. For the tracks processed using topsStack (Aqaba and Australia), the lack of accounting for the burst geometry results in small discontinuities in the velocity field at the burst boundaries in the final velocity field, which can be seen on close inspection of Figures S2-S5. These discontinuities are below the 1 mm/yr level, and are short-wavelength ramps within the bursts, meaning they do not affect the long-wavelength velocity field.

If there are errors in the long-wavelength ionospheric phase removal, and these errors are proportional to the size of the ionospheric signal, they could be revealed by differences in the long-wavelength residual velocity field between ascending and descending tracks covering the same region. For both Makran and Aqaba, there do not seem to be substantial differences in the long-wavelength residuals between the ascending and descending tracks that could reasonably be attributed to uncompensated ionosphere. These results suggest that the ionosphere corrections are able to remove a substantial fraction of the long-wavelength ionospheric signal, but we are not able to precisely quantify the residual long-wavelength ionosphere.

Unlike ionospheric signals, the tropospheric phase is dominated by seasonal variability, meaning longer time series will reduce the tropospheric effect on the estimated secular velocity (Fattahi & Amelung, 2015; Parizzi et al., 2021). The troposphere signal varies depending on the location, but can have an amplitude equivalent to tens of centimeters

of ground deformation. This signal can be mitigated, but not eliminated, by tropospheric models (Fattahi & Amelung, 2015; Bekaert et al., 2015; Parizzi et al., 2021). Fattahi and Amelung (2015) examined the tropospheric noise just to the west of the Makran subduction zone, finding that, after corrections with the ERA-Interim weather model, the tropospheric delay would lead to uncertainties in the InSAR-derived velocities of 2 mm/yr over 100km and 4 mm/yr over 400km with 7 years of Envisat data. Parizzi et al. (2021) evaluated the tropospheric contribution to InSAR-derived velocity uncertainties for locations including the Makran and Gulf of Aqaba. They estimated that uncertainties were in the range 2-4 mm/yr over 150 km for the Makran, and 1-2 mm/yr over 150 km in the Gulf of Aqaba, using at least four years of Sentinel-1 data and corrections from the ERA5 weather model from ECMWF. They stated that tropospheric signals are the limiting factor for measuring large-scale deformation using InSAR, as the residuals from the ionosphere and solid Earth tides are negligible after correction, and the contribution of orbital errors is also not significant compared with the troposphere.

Our data spans 5-7 years, with 150-200 acquisitions per track (Table S1), and we use the ERA5 weather model in our corrections (Hersbach et al., 2020). We therefore expect the contribution of the troposphere to the velocity field to be at or below the levels outlined by Parizzi et al. (2021) for Makran and Aqaba, but we have not directly estimated this for our data. We also do not have comparable estimates for the Australian tracks.

Tracks in the same region acquired at the same time of day should have statistically similar tropospheric signals in terms of the amplitude and spatial correlation of the phase in each acquisition. Tropospheric signals can therefore create similar InSAR velocity uncer-



tainties for nearby tracks (e.g. Fattahi and Amelung (2015)). However, the troposphere is uncorrelated at timescales longer than a day (Emardson et al., 2003), meaning tracks in the same region whose acquisitions are separated by more than a day (as is the case for all of our tracks in the same region) will have different realisations of the tropospheric phase in each acquisition. We would therefore expect the long-wavelength velocity residuals from the troposphere to be different for each track in a given region, rather than systematically contributing velocity ramps in a particular direction. This expectation also applies to tropospheric residuals that remain after troposphere corrections have been applied.

Orbital errors can also create long-wavelength artefacts in individual interferograms, which can impact the velocity estimate. Fattahi and Amelung (2014) found that for Sentinel-1, orbital errors would lead to velocity uncertainties at the level of 0.5 mm/yr over 100 km, assuming 15 acquisitions per year for 8 years. Similarly to the troposphere, we would expect the orbital error to have different realisations in each track, meaning that the velocity ramps from orbital errors would not be expected to occur systematically in any particular direction.

The solid Earth tides (SET) are another long-wavelength signal. SET can contribute along-track InSAR phase ramps, and the varying satellite line-of-sight (LOS) will also mean that SET deformation creates ramps in the range direction as well (Xu & Sandwell, 2020), in a similar fashion to the LOS projection of plate motion. The SET are periodic, and the Sentinel-1 sampling frequency causes diurnal and semi-diurnal tidal periods to be aliased to longer periods of up to a year (Xu & Sandwell, 2020). Using multi-year time

series reduces the influence of these periodic terms on the secular velocity estimation. The SET estimate is accurate to better than 1 mm (Petit & Luzum, 2010), so after correction we expect its residual contribution to the long-wavelength velocity to be much smaller than other signals discussed here.

We do not correct for the deformation due to ocean tidal loading (OTL) in this work (Dicaprio et al., 2008). OTL is a periodic, long-wavelength signal, much like the SET, and the satellite LOS variation causes changing sensitivity to this deformation in the range direction. The periodic nature of the signal means that it will cause a smaller bias in the estimated secular velocity in longer time series (Yu et al., 2020), similarly to the SET. We expect deformation due to OTL to decay with distance from the ocean, meaning the direction and magnitude of any long-wavelength velocity residuals due to OTL will be different for each of our regions. Yu et al. (2020) identified regions of the Earth where OTL corrections would be significant for reducing long-wavelength residuals (see Figure 1 in Yu et al. (2020)). As all of our study areas lie outside these regions, we believe that the OTL signal will have a smaller influence on the velocity than corrections such as the ionosphere, troposphere and plate motion, but may be comparable to the SET, particularly for the Makran.

The DEM error signal is generally short wavelength, as well as depending on the satellite baseline (Fattahi & Amelung, 2013), which is well controlled for Sentinel-1 (Li et al., 2016) and varies largely randomly in time. The DEM error signal is estimated from correlation between the perpendicular baseline and time series residuals, meaning that large residuals from other sources, such as the troposphere, can potentially bias the DEM error estimation

(Fattahi & Amelung, 2013). It is possible that we see this biasing in Figure 2(i) at around (26°N, 60°E), but the impact is still small, at around 0.5 mm/yr over 100 km. Even with the biasing from residual troposphere, we expect residual long-wavelength noise from DEM error to be well below residuals from other sources after correction.

Decorrelation is an additional source of noise in InSAR measurements (Zebker & Villasenor, 1992). Changes in the surface properties can alter the interferometric phase, which causes noise in the estimates of the deformation time series and thus greater errors in the calculated secular velocity. We do not expect this noise source to vary systematically over long distances, so it is unlikely to create significant biases in the long-wavelength velocity field. The impact of decorrelation can be seen by comparing tracks from Australia and the Makran. Lower coherence of the Australian interferograms compared with the Makran causes the Australian track velocity profiles to have a larger scatter in the velocities (Figure 4).

Another source of noise comes from the closure phase introduced as a result of multi-looking combined with phase-changing physical processes on the Earth’s surface (Ansari et al., 2021; Zheng et al., 2022). While this can bias velocity estimates, we would not expect to see systematic spatial biases in the velocity over hundreds of kilometers, so we do not expect this signal to contribute substantially to the long-wavelength velocity field.

Even when a term does not contribute to the long-wavelength velocity field (say, varying on a scale of well under 100 km), it can still bias the estimate of the across track ramp, with the bias being more pronounced for shorter tracks. It is possible that this explains the larger residual across track ramp for track 46 (Australia). This track is the shortest in

our data set, and also has the largest across track residual after plate motion correction, at 1.5 mm/yr/track. For longer tracks, the bias on the ramp estimation by short-wavelength terms is reduced. This reduction in bias is similar to longer time series having a secular velocity that is less biased by periodic terms.

The expected amplitude and spatial wavelength of the residuals discussed above, as well as the consistency between multiple tracks, including ascending and descending tracks covering the same area, gives additional credence to the claim that the long-wavelength range-dependent ramps that we observe in our data after applying corrections are primarily due to plate motion. Plate motion and ionosphere are the two signals that have secular trends over several years, whereas signals such as the troposphere and SET are dominated by seasonal variations. It is this temporal variation that explains why the ionosphere and plate motion are dominant contributors to the long-wavelength velocities in our multi-year time series, while the large amplitude of troposphere variation results in it also contributing substantially.

### **Text S3: Further Details on the Signal of Vertical and Horizontal Plate Motions in InSAR Measurements**

In Figure S6 we show estimates of the scale of the velocity ramp in the satellite range direction for given vertical or horizontal plate translation. The values are calculated by subtracting the LOS projection of plate motion in the satellite far range from the projection in satellite the near range (see Figure 1, but note that the ramps in Figure 1 are plotted as a function of distance along the ground (ground range), not distance from the satellite (slant range)). These plots can be used for an estimate of the expected

InSAR-derived velocity ramps given values of the plate motion velocity. Figure S6 shows that, for a given plate speed, the impact on the LOS velocity is largest when the plate is moving parallel to the heading angle of the LOS vector (i.e. approximately perpendicular to the satellite direction of motion). Note that in Figure S6 we use the line-of-sight vectors from the ascending and descending tracks over Aqaba (track 87 and track 21 respectively). While the pattern of LOS incidence angle variation across the track will be very similar for all tracks acquired in interferometric wideswath mode, the satellite orbit heading angle (and therefore the LOS heading angle) will vary with latitude due to the near-polar orbit of the Sentinel-1 satellites. The LOS heading angle also has a small variation across the track, which can be seen from the LOS geometry files (not shown here). Users should therefore examine the true LOS vector for their study area, and only use Figure S6 for a quick estimate of the ramps they could expect in their study regions.

Vertical secular bulk motion will have a different signature in ASC and DSC tracks compared to horizontal secular velocity. For horizontal plate motion to the east, for example, the ASC track will have a line of sight velocity gradient that is negative with increasing range and the descending track will have the opposite, assuming a right-looking satellite such as Sentinel-1 (Figure S6). When translated into geographic coordinates, this will result in both ASC and DSC tracks having negative velocity gradients to the east (Figure 1). In contrast, a constant, positive, vertical velocity will appear as negative LOS velocity gradients in range for ASC and DSC, which translates to a negative LOS velocity gradient to the east in the ASC track and a positive gradient to the east in the DSC track. The gradients would be reversed for negative vertical velocities. This effect is illustrated

in Figure 1(c), and we show examples of the ramp sizes for varying horizontal and vertical plate motion in Figure S6.

Altamimi et al. (2017) and Altamimi et al. (2012) have noted that plate motion models may be contaminated by the inclusion of stations undergoing glacial isostatic adjustment (GIA). Therefore it may not be appropriate to investigate GIA by subtracting a plate motion model from a velocity field, and a more careful investigation of the local velocity field might be warranted.

As suggested in the Conclusion, the signal of plate motion in InSAR data could be used to better constrain plate motion models. This could be limited to constraining horizontal plate motions, but if the direction of horizontal plate motion is known, then the velocity gradients of ascending and descending tracks combined could potentially be used to constrain the amplitude of horizontal and vertical plate motions together. Such constraints could prove useful for improving plate models, particularly where GNSS points are sparse. However, this approach could prove challenging if there was substantial contributions from noise sources and tectonic deformation, and would likely require long InSAR time series to reduce the biasing of the velocity by non-secular terms, and long tracks to avoid biasing by short-wavelength velocity residuals.

#### **Text S4: The Impact of Plate Motion on 3D Velocity Fields Derived from InSAR**

While individual InSAR tracks only provide one line-of-sight for each point on the ground, multiple tracks with different LOS angles can be combined to constrain the 3D velocity field (Fialko et al., 2001; Wright et al., 2004). When a ascending and descending

track covering the same region are available, these can be used to derive the horizontal and vertical velocities by assuming the direction of the horizontal velocity, and choosing the same reference point for both of these tracks, which is implicitly assumed to be stable in the reference frame of the satellite (e.g. Wright et al. (2004)). By assuming that this point is stable, we further assume that the ascending and descending track velocities can be explained purely by motions relative to this point, which means our solution cannot contain any overall translation. The assumption of a constant horizontal velocity direction also prohibits any rotational component in our inferred velocities. If there is in fact an overall translation or rotation of our observed region, this could lead to a biasing of our calculated horizontal and vertical velocities.

In Figure S7, we illustrate how plate motion biases our estimation of the 3D velocity field. We use the overlapping region of tracks 86 and 20 over the Makran subduction zone, and first apply the corrections shown in Figures 2 and S1, (f)-(i), to each tracks 86 and 20 respectively. Using these two lines of sight we then calculate the horizontal and vertical velocities, assuming that horizontal velocity is purely due east. When we perform this calculation before plate motion correction, the east and vertical components contain long-wavelength velocity ramps (Figure S7 (a)-(b)). The vertical velocity has a ramp of around 3 mm/yr/100 km in the east-west direction, and the eastward velocity has a ramp of approximately 1.5 mm/yr/100 km in the north-south direction. These velocity ramps are primarily a bias from plate motion combined with the assumption that the reference point is fixed.

After removing the plate motion contribution to the ascending and descending tracks and repeating the calculation, the long-wavelength velocity ramps in the calculated horizontal and vertical maps are substantially reduced (Figure S7 (c)-(d)). There may be some remaining bias from the assumption that horizontal motion is purely east-west.

The bias from plate motion would not be present if the InSAR observations had had a ramp fitted and removed before the calculation (as is often done), as this would remove the plate motion velocity ramp. The bias would also be less obvious if the area studied was smaller, or the tectonic signal was larger. The results in Figure S7 emphasize the importance of accounting for the reference frame of our observations before combining separate tracks.

## References

- Altamimi, Z., Métivier, L., & Collilieux, X. (2012). ITRF2008 plate motion model. *Journal of Geophysical Research: Solid Earth*, 117(7), 1–14. doi: 10.1029/2011JB008930
- Altamimi, Z., Métivier, L., Rebischung, P., Rouby, H., & Collilieux, X. (2017). ITRF2014 plate motion model. *Geophysical Journal International*, 209(3), 1906–1912. doi: 10.1093/gji/ggx136
- Ansari, H., De Zan, F., & Parizzi, A. (2021). Study of Systematic Bias in Measuring Surface Deformation with SAR Interferometry. *IEEE Transactions on Geoscience and Remote Sensing*, 59(2), 1285–1301. doi: 10.1109/TGRS.2020.3003421
- Bekaert, D., Walters, R., Wright, T., Hooper, A., & Parker, D. (2015). Statistical comparison of InSAR tropospheric correction techniques. *Remote Sensing of Environment*, 170, 40–47. Retrieved from <https://linkinghub.elsevier.com/retrieve/pii/>



S0034425715301231 doi: 10.1016/j.rse.2015.08.035

Berardino, P., Fornaro, G., Lanari, R., & Sansosti, E. (2002). A new algorithm for surface deformation monitoring based on small baseline differential SAR interferograms. *IEEE Transactions on Geoscience and Remote Sensing*, 40(11), 2375–2383. Retrieved from <http://ieeexplore.ieee.org/document/1166596/> doi: 10.1109/TGRS.2002.803792

Chen, C. W., & Zebker, H. A. (2002). Phase unwrapping for large SAR interferograms: Statistical segmentation and generalized network models. *IEEE Transactions on Geoscience and Remote Sensing*, 40(8), 1709–1719. doi: 10.1109/TGRS.2002.802453

De Zan, F., Prats-Iraola, P., Scheiber, R., & Rucci, A. (2014). Interferometry with TOPS: Coregistration and azimuth shifts. *Proceedings of the European Conference on Synthetic Aperture Radar, EUSAR, Proceeding(0)*, 949–952.

Dicaprio, C. J., Simons, M., Kenner, S. J., & Williams, C. A. (2008). Post-seismic reloading and temporal clustering on a single fault. *Geophysical Journal International*, 172(2), 581–592. doi: 10.1111/j.1365-246X.2007.03622.x

Emardson, T. R., Simons, M., & Webb, F. H. (2003). Neutral atmospheric delay in interferometric synthetic aperture radar applications: Statistical description and mitigation. *Journal of Geophysical Research: Solid Earth*, 108(B5), 1–8. Retrieved from <http://doi.wiley.com/10.1029/2002JB001781> doi: 10.1029/2002JB001781

Fattahi, H., Agram, P., & Simons, M. (2017). A Network-Based Enhanced Spectral Diversity Approach for TOPS Time-Series Analysis. *IEEE Transactions on Geoscience and Remote Sensing*, 55(2), 777–786. Retrieved from <http://ieeexplore.ieee.org/>

document/7637021/ doi: 10.1109/TGRS.2016.2614925

Fattahi, H., & Amelung, F. (2013). DEM Error Correction in InSAR Time Series. *Geoscience and Remote Sensing, IEEE Transactions on*, 51(7), 4249–4259. Retrieved from <http://ieeexplore.ieee.org/document/6423275/> doi: 10.1109/TGRS.2012.2227761

Fattahi, H., & Amelung, F. (2014). InSAR uncertainty due to orbital errors. *Geophysical Journal International*, 199(1), 549–560. doi: 10.1093/gji/ggu276

Fattahi, H., & Amelung, F. (2015). InSAR bias and uncertainty due to the systematic and stochastic tropospheric delay. *Journal of Geophysical Research: Solid Earth*, 120(12), 8758–8773. Retrieved from <https://onlinelibrary.wiley.com/doi/abs/10.1002/2015JB012419> doi: 10.1002/2015JB012419

Fattahi, H., Simons, M., & Agram, P. (2017). InSAR Time-Series Estimation of the Ionospheric Phase Delay: An Extension of the Split Range-Spectrum Technique. *IEEE Transactions on Geoscience and Remote Sensing*, 55(10), 5984–5996. doi: 10.1109/TGRS.2017.2718566

Fialko, Y., Simons, M., & Agnew, D. (2001). The complete (3-D) surface displacement field in the epicentral area of the 1999 Mw 7.1 Hector Mine earthquake, California, from space geodetic observations. *Geophysical Research Letters*, 28(16), 3063–3066. doi: 10.1029/2001GL013174

Gomba, G., Parizzi, A., De Zan, F., Eineder, M., & Bamler, R. (2016). Toward operational compensation of ionospheric effects in SAR interferograms: The split-spectrum method. *IEEE Transactions on Geoscience and Remote Sensing*, 54(3), 1446–1461.

doi: 10.1109/TGRS.2015.2481079

- Hersbach, H., Bell, B., Berrisford, P., Hirahara, S., Horányi, A., Muñoz-Sabater, J., ... Thépaut, J. (2020). The ERA5 global reanalysis. *Quarterly Journal of the Royal Meteorological Society*, 146(730), 1999–2049. Retrieved from <https://onlinelibrary.wiley.com/doi/10.1002/qj.3803> doi: 10.1002/qj.3803
- Jolivet, R., Agram, P. S., Lin, N. Y., Simons, M., Doin, M.-p., Peltzer, G., & Li, Z. (2014). Improving InSAR geodesy using Global Atmospheric Models. *Journal of Geophysical Research: Solid Earth*, 119(3), 2324–2341. Retrieved from <https://onlinelibrary.wiley.com/doi/abs/10.1002/2013JB010588> doi: 10.1002/2013JB010588
- Jolivet, R., Grandin, R., Lasserre, C., Doin, M. P., & Peltzer, G. (2011). Systematic InSAR tropospheric phase delay corrections from global meteorological reanalysis data. *Geophysical Research Letters*, 38(17), 1–6. doi: 10.1029/2011GL048757
- Li, Z., Wright, T., Hooper, A., Crippa, P., Gonzalez, P., Walters, R., ... Parsons, B. (2016). Towards InSAR everywhere, all the time, with Sentinel-1. *International Archives of the Photogrammetry, Remote Sensing and Spatial Information Sciences - ISPRS Archives*, 41(July), 763–766. doi: 10.5194/isprsarchives-XLI-B4-763-2016
- Liang, C., Agram, P., Simons, M., & Fielding, E. J. (2019). Ionospheric Correction of InSAR Time Series Analysis of C-band Sentinel-1 TOPS Data. *IEEE Transactions on Geoscience and Remote Sensing*, 57(9), 6755–6773. doi: 10.1109/tgrs.2019.2908494
- Liang, C., Liu, Z., Fielding, E. J., & Bürgmann, R. (2018). InSAR time series analysis of L-Band wide-swath SAR data acquired by ALOS-2. *IEEE Transactions on Geoscience and Remote Sensing*, 56(8), 4492–4506. doi: 10.1109/TGRS.2018.2821150

- Milbert, D. (2018). *solid: Solid Earth Tide*. Retrieved from <https://geodesyworld.github.io/SOFTS/solid.htm>
- Parizzi, A., Brcic, R., & De Zan, F. (2021). InSAR Performance for Large-Scale Deformation Measurement. *IEEE Transactions on Geoscience and Remote Sensing*, 59(10), 8510–8520. doi: 10.1109/TGRS.2020.3039006
- Petit, G., & Luzum, B. (2010). *IERS Conventions (IERS Technical Note No. 36)*. Frankfurt, Germany. Retrieved from <http://www.iers.org/TN36/>
- Rosen, P. A., Gurrola, E., Sacco, G. F., & Zebker, H. (2012). The InSAR scientific computing environment. In *Proceedings of the european conference on synthetic aperture radar, eusar* (Vol. 2012-April, pp. 730–733).
- Wright, T. J., Parsons, B. E., & Lu, Z. (2004). Toward mapping surface deformation in three dimensions using InSAR. *Geophysical Research Letters*, 31(1), 1–5. doi: 10.1029/2003GL018827
- Xu, X., & Sandwell, D. T. (2020). Toward Absolute Phase Change Recovery with InSAR: Correcting for Earth Tides and Phase Unwrapping Ambiguities. *IEEE Transactions on Geoscience and Remote Sensing*, 58(1), 726–733. doi: 10.1109/TGRS.2019.2940207
- Yu, C., Penna, N. T., & Li, Z. (2020). Ocean Tide Loading Effects on InSAR Observations Over Wide Regions. *Geophysical Research Letters*, 47(15). doi: 10.1029/2020GL088184
- Yunjun, Z., Fattahi, H., & Amelung, F. (2019). Small baseline InSAR time series analysis: Unwrapping error correction and noise reduction. *Computers and Geo-*

*sciences*, 133(May), 104331. Retrieved from <https://doi.org/10.1016/j.cageo.2019.104331> doi: 10.1016/j.cageo.2019.104331

Yunjun, Z., Fattahi, H., Pi, X., Rosen, P., Simons, M., Agram, P., & Aoki, Y. (2022). Range Geolocation Accuracy of C/L-band SAR and its Implications for Operational Stack Coregistration. *IEEE Transactions on Geoscience and Remote Sensing*, 2892(c), 1–1. Retrieved from <https://ieeexplore.ieee.org/document/9759304/> doi: 10.1109/TGRS.2022.3168509

Zebker, H. A., & Villasenor, J. (1992). Decorrelation in interferometric radar echoes. *IEEE Transactions on Geoscience and Remote Sensing*, 30(5), 950–959. doi: 10.1109/36.175330

Zheng, Y., Fattahi, H., Agram, P., Simons, M., & Rosen, P. (2022). On Closure Phase and Systematic Bias in Multilooked SAR Interferometry. *IEEE Transactions on Geoscience and Remote Sensing*, 60, 1–11. Retrieved from <https://ieeexplore.ieee.org/document/9758802/> doi: 10.1109/TGRS.2022.3167648

**Table S1.** Summary of Sentinel-1 SAR Data used. ASC: Ascending track. DSC: Descending track. Aqn. no.: Number of acquisitions. Makran and Aqaba use only Sentinel-1A data, Australia uses only Sentinel-1B. The plates used for plate motion corrections are listed in the final column and are taken from Table 1 of Altamimi et al. (2017).

<b>Region</b>	<b>Track</b>	<b>Direction</b>	<b>Start date</b>	<b>End date</b>	<b>Aqn. no.</b>	<b>Plate</b>
Makran	86	ASC	20141023	20210401	158	EURA
Makran	20	DSC	20141007	20210328	150	EURA
Aqaba	87	ASC	20141104	20220102	203	ARAB
Aqaba	21	DSC	20150815	20210503	160	ARAB
Australia	46	DSC	20161003	20211212	157	AUST
Australia	119	DSC	20160926	20211217	158	AUST

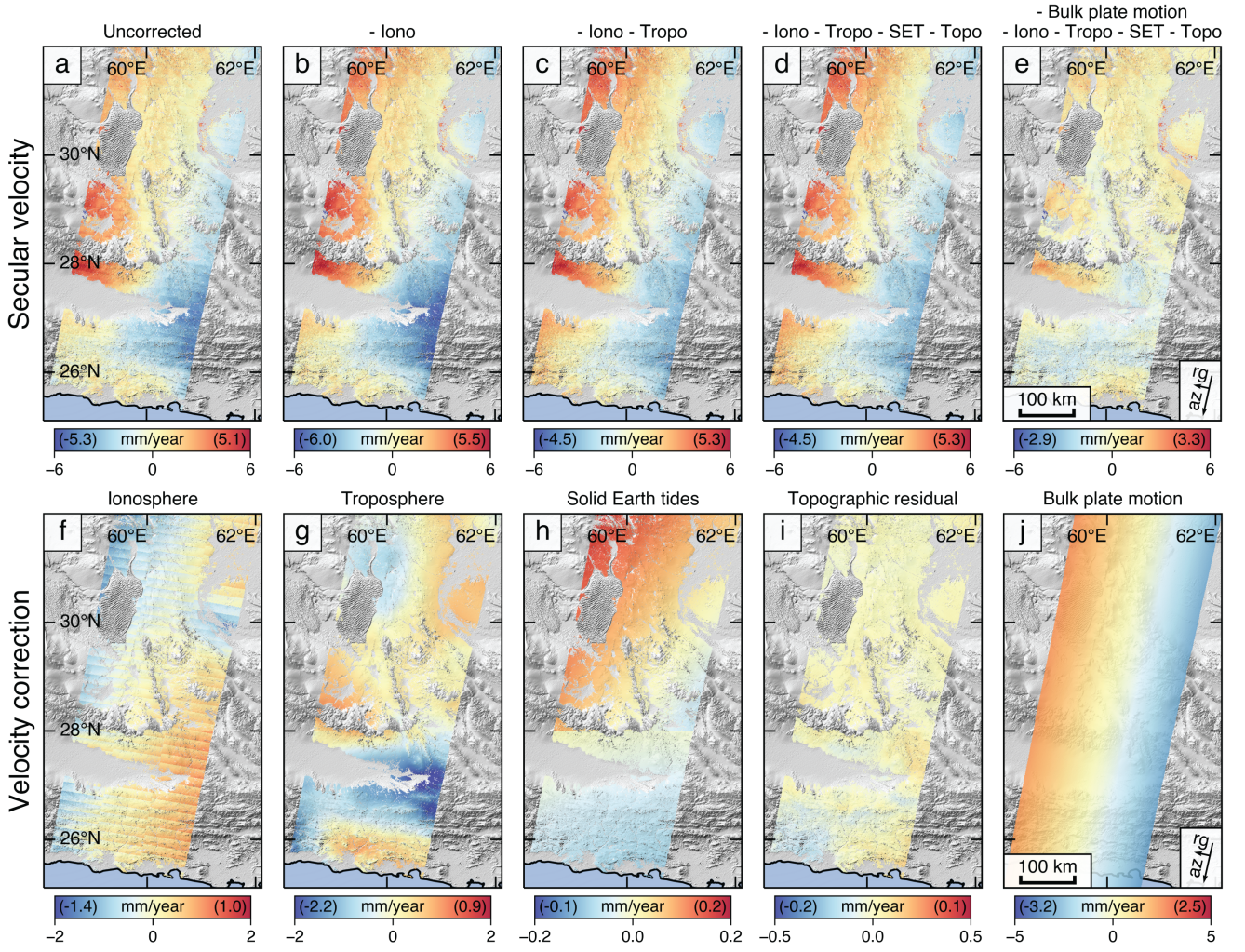


**Figure S1.** Cumulative impact of corrections on the InSAR-derived velocity field for Sentinel-1, track 20 (DSC) over the Makran subduction zone. Panels are as described in Figure 2. Note the substantial difference in the long-wavelength ionospheric correction between ASC (Figure 2(f)) and DSC tracks ((f)). The burst discontinuities due to the ionosphere can be clearly seen in (f) (Liang et al., 2019).



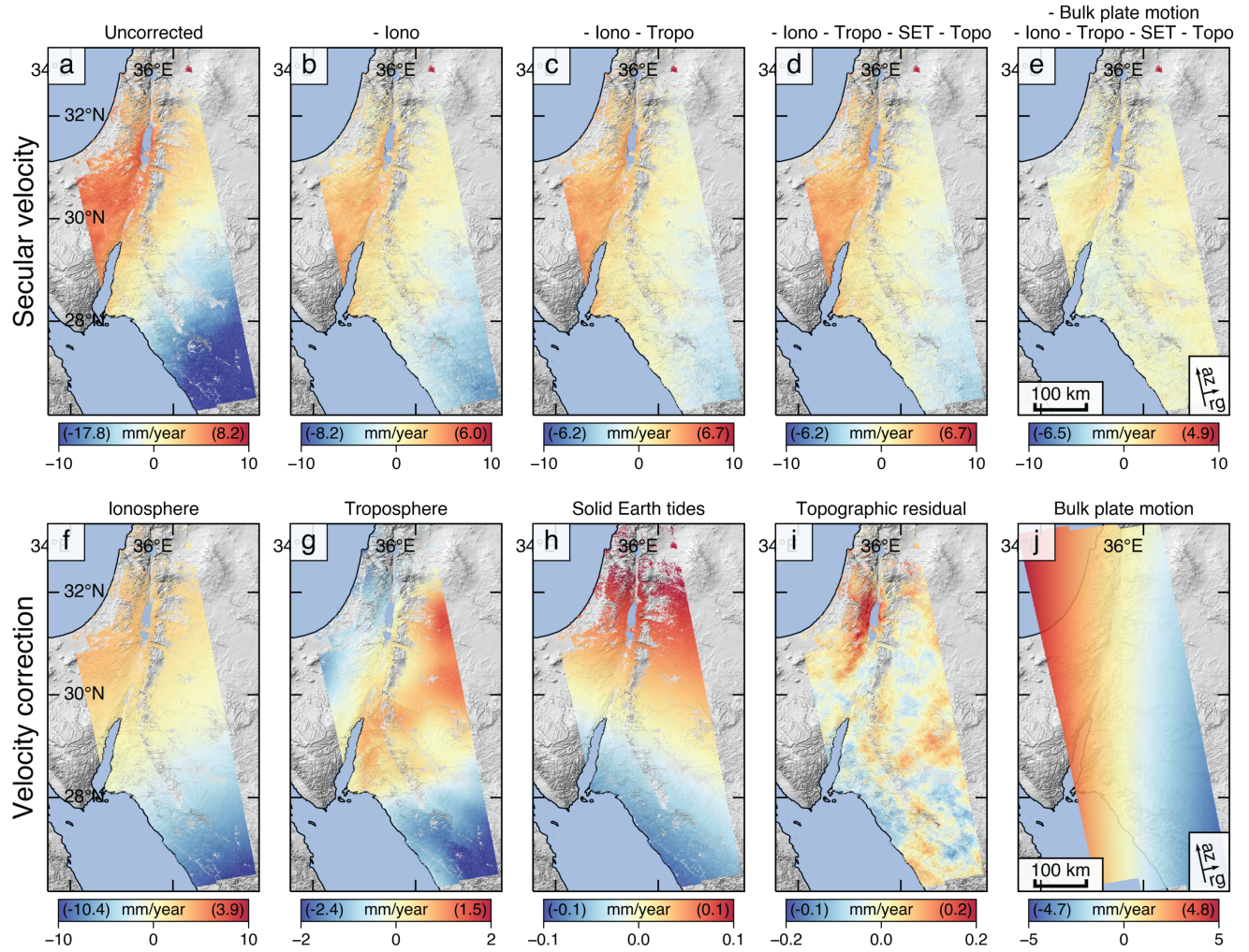


**Figure S2.** Cumulative impact of corrections on the InSAR-derived velocity field for Sentinel-1, track 87 (ASC) over the Gulf of Aqaba. Panels are as described in Figure 2.



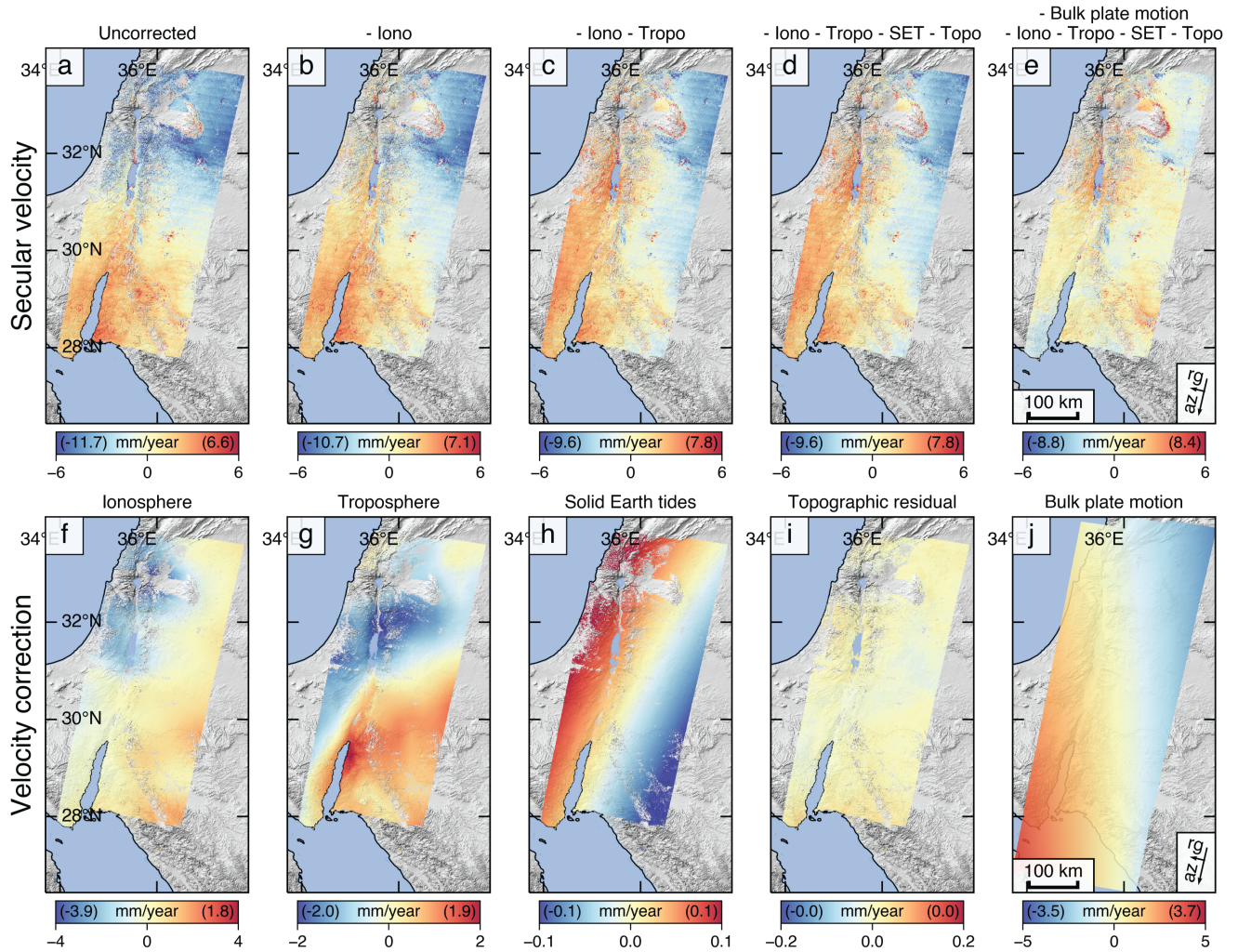


**Figure S3.** Cumulative impact of corrections on the InSAR-derived velocity field for Sentinel-1, track 21 (DSC) over the Gulf of Aqaba. Panels are as described in Figure 2.

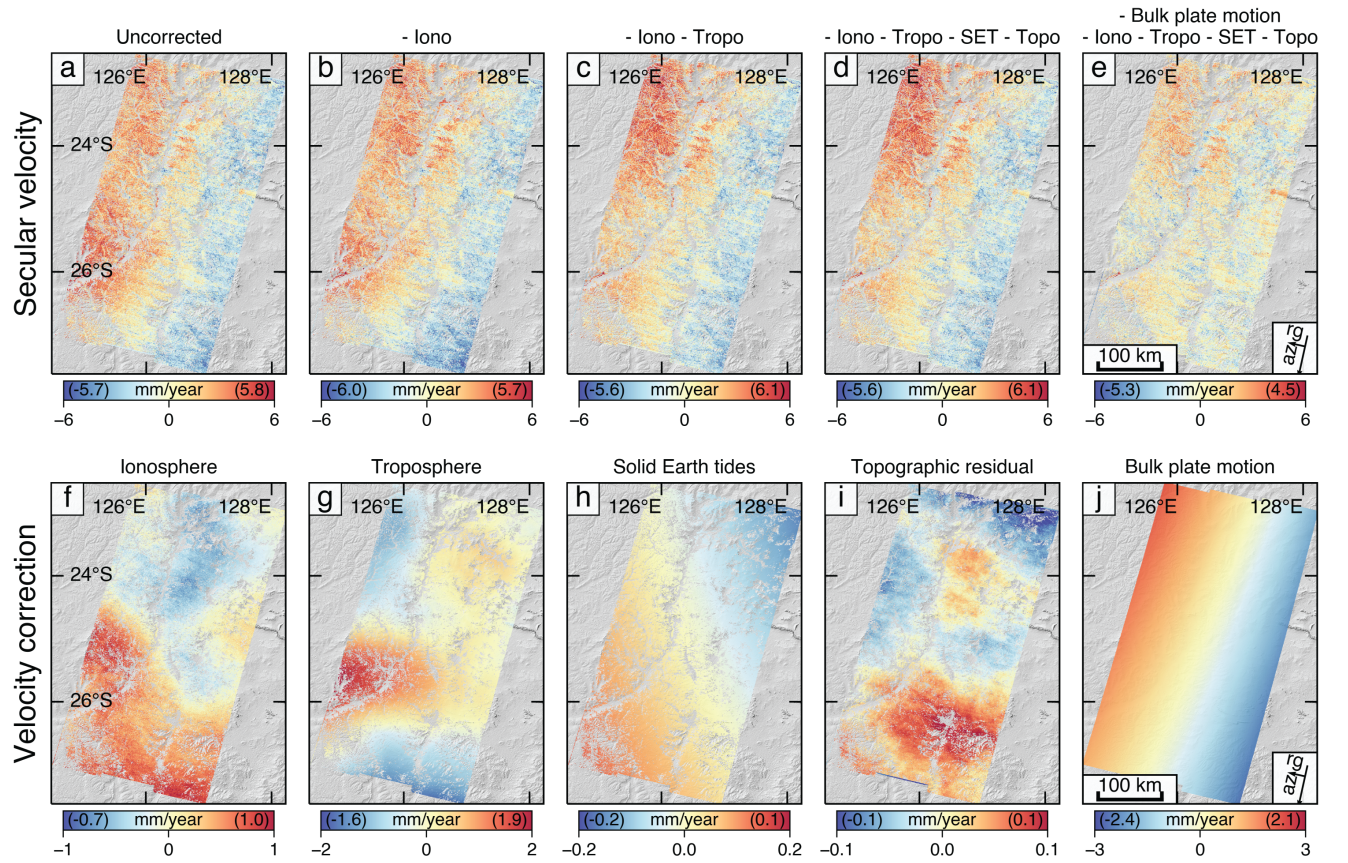


**Figure S4.** Cumulative impact of corrections on the InSAR-derived velocity field for Sentinel-1, track 46 (DSC) over western Australia. Panels are as described in Figure 2.



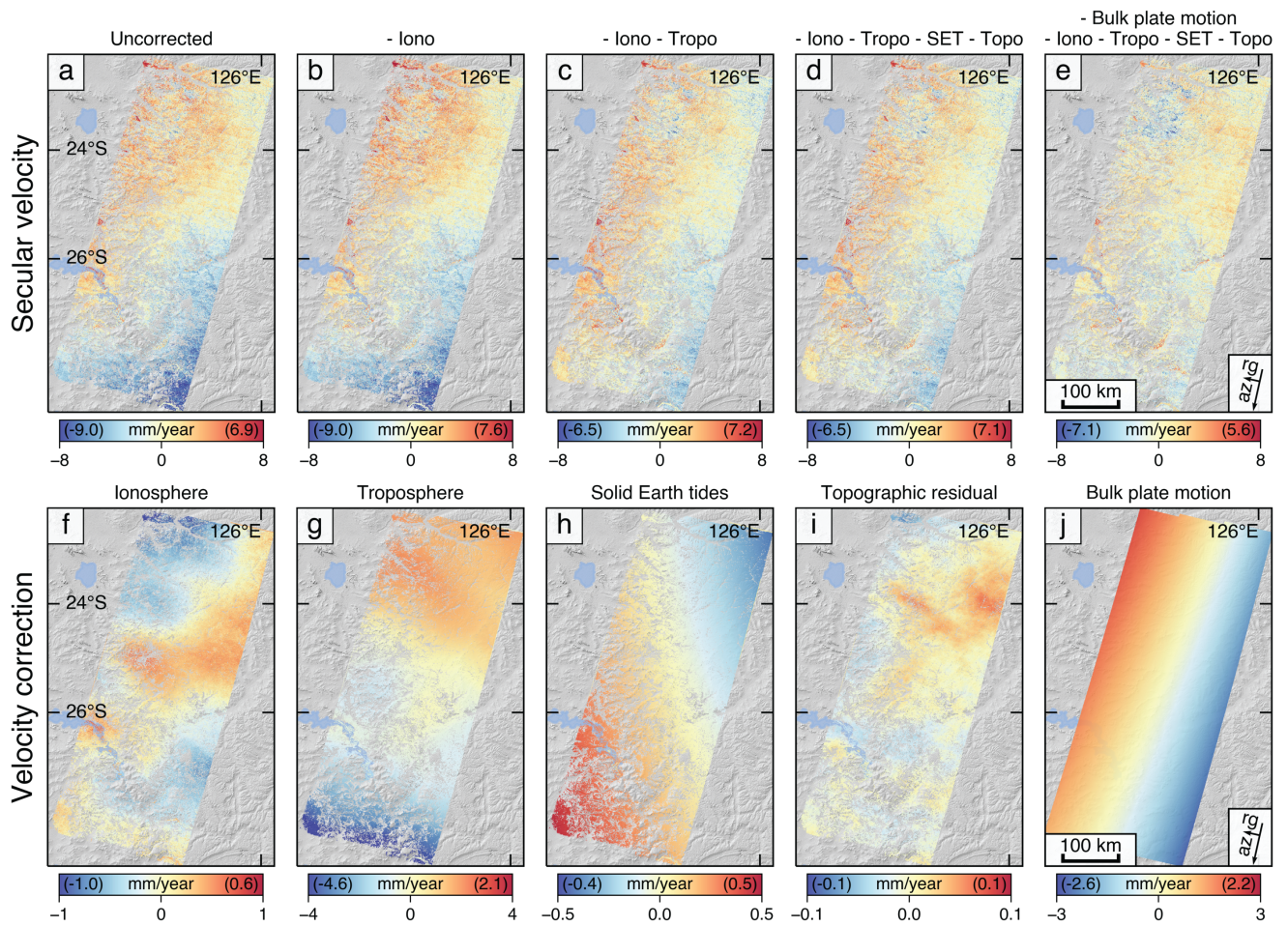


**Figure S5.** Cumulative impact of corrections on the InSAR-derived velocity field for Sentinel-1, track 119 (DSC) over western Australia. Panels are as described in Figure 2.

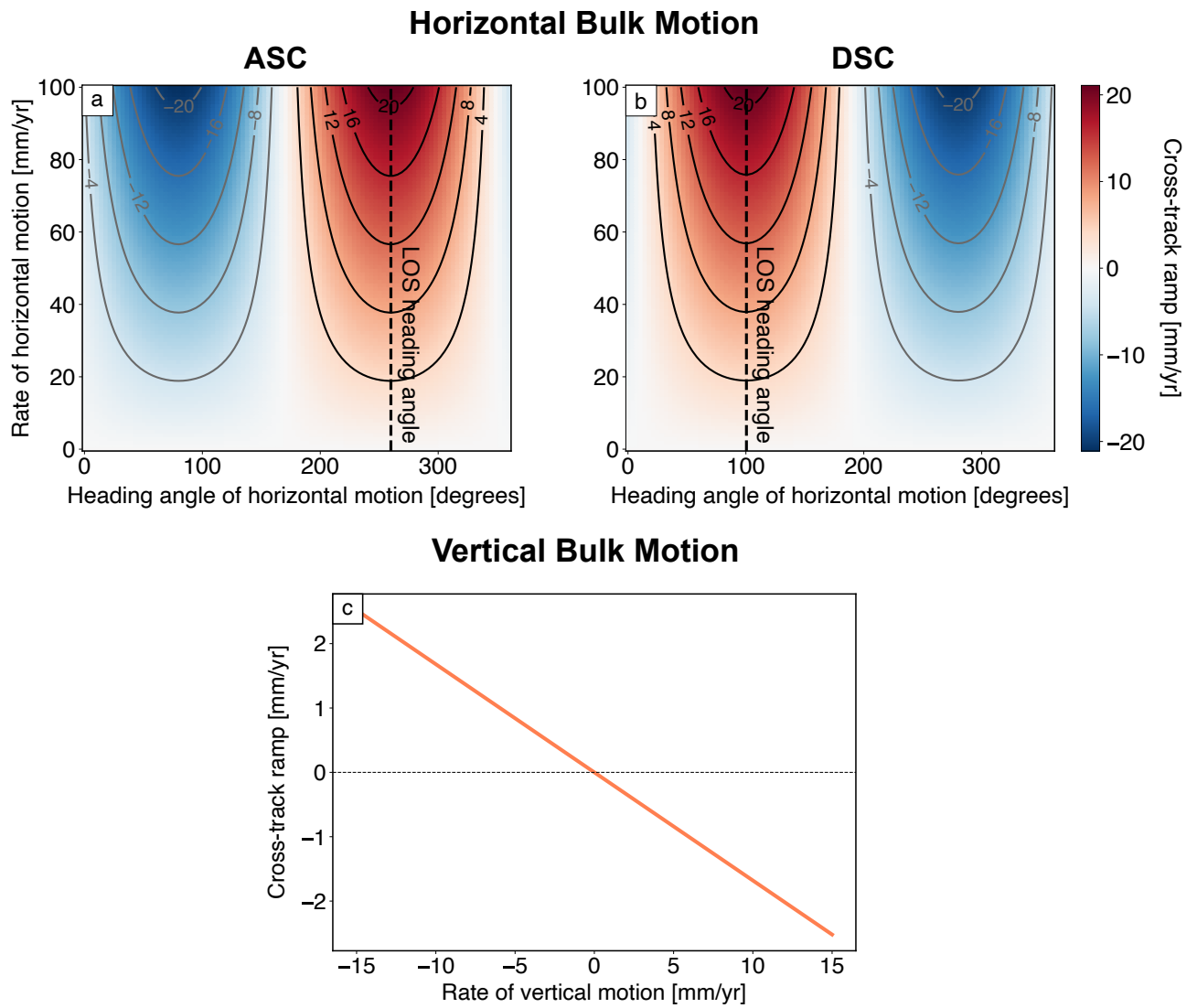


**Figure S6.** Size of velocity ramp in range for the 250 km wide Sentinel-1 swath for varying horizontal and vertical bulk motion. These calculations assume a constant plate velocity (i.e. no rotation), ignore the slight curvature in the across-track ramps (Figure 1), and take the LOS geometry from the ASC and DSC Sentinel-1 tracks over Aqaba (87 and 21 respectively). The LOS vector points from the ground to the satellite. Heading angles are measured clockwise from north. “LOS heading angle” is the heading angle of the horizontal projection of the LOS vector. “Heading angle of horizontal motion” is the heading angle of the bulk plate motion. A positive cross-track ramp means that LOS velocity increases with increasing satellite range. **(a)** Size of velocity ramp for horizontal motion in an ASC track. **(b)** Size of velocity ramp for horizontal motion in a DSC track. **(c)** Size of velocity ramp for vertical velocity motion. For vertical motion, the ramp has the same variation with range for ASC and DSC tracks.

May 30, 2022, 11:41pm

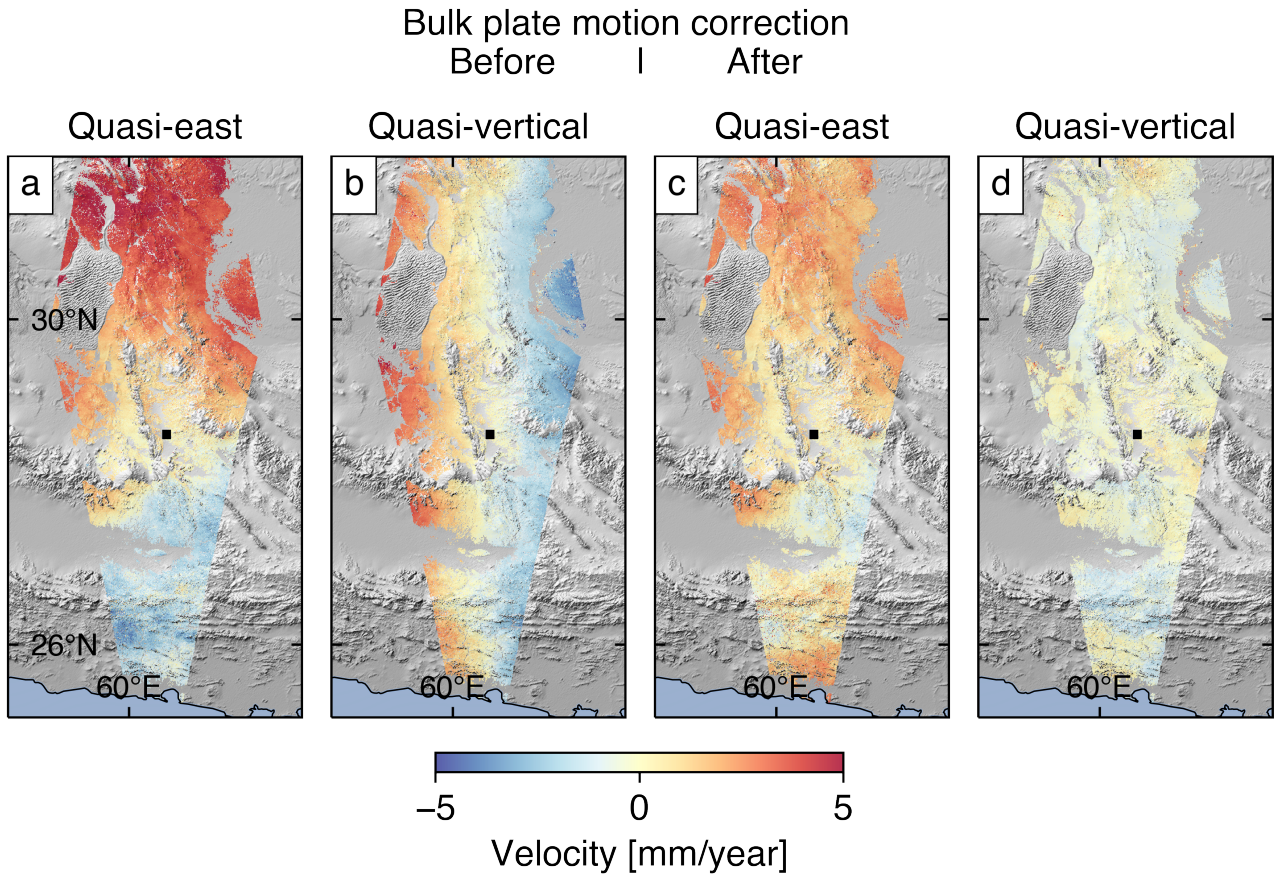


**Figure S7.** Impact of accounting for plate motion on the calculation of horizontal and vertical velocities from ASC and DSC tracks. The calculation is performed for the overlapping region between tracks 86 (ASC) and 20 (DSC) over the Makran subduction zone, with horizontal motion assumed to be purely east-west. The black square represents the reference point, which is assumed to be stationary with respect to the satellite. **(a)** Calculated eastward motion before plate motion correction, but after other corrections have been applied. Note the apparent north-south velocity gradient. **(b)** Calculated vertical motion before plate motion correction. Note the apparent east-west velocity gradient. **(c)**, **(d)** Same as (a) and (b) respectively, but with the plate motion correction applied to each track before calculating the horizontal and vertical terms. Long wavelength velocity gradients have been substantially reduced.